Engineering Structures 199 (2019) 109606

Contents lists available at ScienceDirect

Engineering Structures

journal homepage: www.elsevier.com/locate/engstruct

Nonlinear stability and buckling analysis of composite functionally graded arches subjected to external pressure and temperature loading

Zhaochao Li*, Junxing Zheng, Zhen Zhang, Hantao He

Department of Civil, Construction and Environmental Engineering, Iowa State University, Town Engineering Building, Ames, IA 50011, United States

ARTICLE INFO

Keywords:
Nonlinear stability
Functionally graded
Arch
Pressure
Thermal field
Numerical verification

ABSTRACT

This paper investigates the nonlinear stability and buckling behavior of the composite functionally graded material (FGM) arches subjected to pressure and temperature loadings. By introducing an admissible displacement function, the total potential energy is expressed explicitly following the thin-walled shell theory. The nonlinear equilibrium equations are calculated by the variation of the potential energy function, and the critical buckling pressure is predicted analytically. The verification is taken by the numerical simulation that traces the pre- and post-buckling equilibrium paths, indicating that the numerical results are in good accordance with the analytical predictions. It is found the temperature rise increases the thermal upward displacement, which is beneficial to the buckling pressure, and reduces Young's modulus, which is unbeneficial to the buckling pressure. Therefore, the buckling pressure is nonlinear to the temperature rise. Finally, a series of parametric evaluations are mainly focused on the effects of volume fraction exponent and temperature rise on the distributions of hoop strain, stress, force and bending moment.

1. Introduction

Arch elements are the basic units in civil infrastructures. The instability behavior of the arch element is common due to its high slenderness ratio, indicating the length is much higher than the dimensions of the cross-section. Therefore, it is significant to study the buckling responses of the arch structures. Existing studies [1–7] found that the buckling performance was induced by excessive hoop stress, which results from the mechanical loadings and/or thermal effects. When the arch buckles, the deformation may be symmetrical or asymmetrical as shown in Fig. 1 [8–10]. In the present investigation, the symmetrical buckling mechanism is mainly concerned, and the asymmetrical buckling mechanism can also be evaluated with a similar derivation procedure. Following the simulation results [11,12], the deformation is sensitive to the initial imperfection, indicating symmetrical initial imperfection results in symmetrical deformed shape and asymmetrical initial imperfection results in asymmetrical deformed shape, respectively.

Functionally graded materials (FGM) have been widely used in recent several decades. The concept of the FGM was proposed to dissipate the heat of the outer surface of the aircraft due to its high performance of thermal resistance [13]. And then, the FGM was extended in many other fields, such as nuclear power plants, thermal power plants and so on. In addition, the FGM was also used in the biological field for artificial bones or teeth, or in deep-sea apparatus for its high strength and corrosion resistance [14]. Many studies were concerned with the stability mechanism of the FGM arches. A typical FGM arch consists of two constituents with ceramic rich in outside surface and metal rich in inside surface as depicted in Fig. 2. Asgari et al. [15] reported the buckling mechanism of the FGM arches under thermal effect. Based on the scheme of virtual displacement, the theoretical prediction of the critical temperature rise was obtained. It was concluded that material failure was prior to the thermal buckling. Bateni and Eslami [16] studied the collapse mechanism of the shallow FGM arches under a radially-directed concentrated load. Both pinned-pinned and clamped-clamped FGM arches were discussed and the buckling load was predicted by solving a set of nonlinear equilibrium equation. Swaminathan et al. [17] presented the buckling mechanism of the FGM plates under different loadings types, boundaries, length-to-width ratios, and length-to-thickness ratios. Simsek [18] examined the two-dimensional Timoshenko FGM beams with the Ritz method. The critical buckling load is predicted by taking polynomial forms of the axial, transverse displacement and rotation of the beam cross-sections. Recently, Moita et al. [19] reported the effect of material distribution on the buckling behavior of the FGM structures based on the theory of higher-order deformation. Five different types of FGM plates and panels were

* Corresponding author.
E-mail address: zhaochao@iastate.edu (Z. Li).

https://doi.org/10.1016/j.engstruct.2019.109606
Received 27 June 2019; Received in revised form 27 July 2019; Accepted 29 August 2019

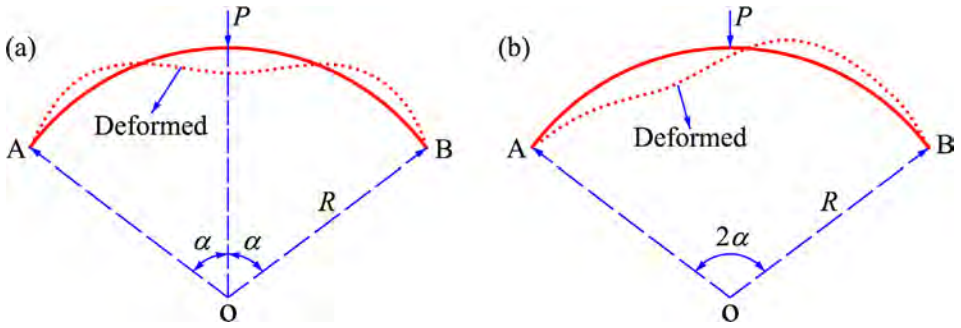

Fig. 1. A homogeneous arch deforms with (a) symmetrical, and (b) asymmetrical shapes.

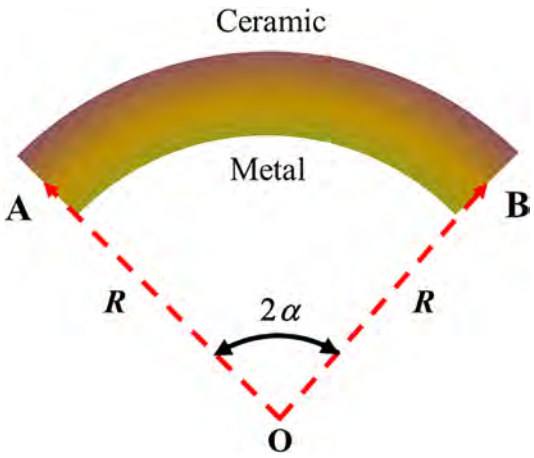

Fig. 2. Material distributions of an FGM arch.

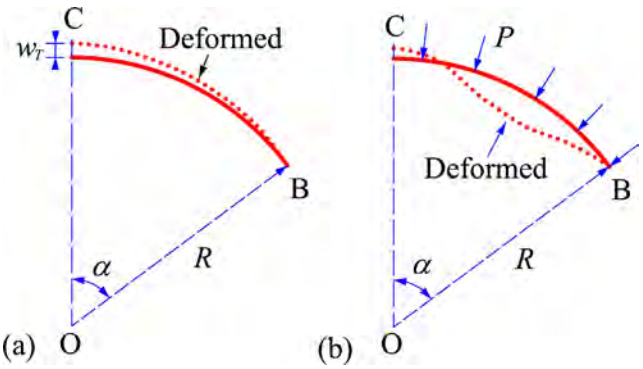

Fig. 3. Deformed shapes of an FGM arch under (a) a temperature rise field, and (b) combined temperature rise field and pressure field.

examined. Al-shujairi and Mollamahmutoğlu [20] examined the buckling performance of FGM sandwich beams under the thermal variational field. The critical buckling load was obtained by using the generalized differential quadrature method.

All the above literature considered the arch was under a single load. In engineering practice, an arch may be subjected to two or more loading effects. Xi and Li [21] investigated a semicircle FGM arch under uniform pressure in a thermal environment. The equilibrium paths were traced numerically. Pi and Bradford [22] studied a homogeneous arch under uniform radial and thermal loading. The critical buckling pressure was obtained analytically and then verified by the numerical simulations. The pressure capacity sustained by the arch was sensitive to the temperature rise. Generally, the conventional approaches of developing the governing equilibrium equations were summarized as static eigenvalue method [23] and energy method [24]. For the eigenvalue method, the geometric nonlinearities were neglected, resulting in an overestimation of the buckling load especially for the very shallow arches [25]. For the energy method, the principle of virtual work was commonly used as Refs. [15,16,22]. Nevertheless, it was difficult to obtain an explicit expression of the buckling load.

When an FGM arch is surrounded by a thermal rise field, a hoop compressive force develops significantly, and an outward displacement (w_T) generates as shown in Fig. 3(a). This thermal displacement (w_T) may result in different defomation and buckling load. Therefore, it is essential to explore the buckling, and the post-buckling behavior of the pressurized FGM arch under the thermal variational field.

The present work focuses on the nonlinear stability mechanism of the pressurized FGM arches in a temperature rise environment. Based on the deformed shape in Fig. 3(b) [26–31], the analytical buckling pressure is derived for both clamped-clamped and pinned-pinned arches. Subsequently, the analytical solution is compared with numerical results for the FGM arch, as well as other closed-form predictions [22] for the homogeneous arch, respectively. In the present numerical model, the geometric nonlinearities are introduced and modified arc-length algorithm is considered to track the pre- and post-buckling equilibrium paths. Finally, the effects of material properties and temperature rise on the internal forces and deformations are examined and discussed.

2. Assumptions and formation of equilibrium equations

The geometric parameters are shown in Fig. 4, with central angle α and its corresponding circumferential length L, where $L = R\alpha$, the cross-section $b \times t$, and the radius R, respectively. An orthogonal curvilinear coordinate system is defined, with x-, y- and z-axes in the tangential, axial, and radial directions, respectively. Two hypotheses are taken to facilitate the derivation process, yielding (1) the dimensions of the cross section $b \times t$ are much smaller than the length ($2L$) and radius (R). Therefore, the cross-section remains in the plane during deformations; and (2) the material properties of the two constituents depend on temperature and only elastic properties are considered. The buckling is prior to the material failure in the present investigation.

As seen in Fig. 4, the radial displacement is defined as $w = w(z, \phi)$ and the tangential displacement is $v = v(z, \phi)$, respectively. Here $s = R\phi$, where ϕ is the angle starting from the crown and works clockwise, and $-1 \le \phi/\alpha \le 1$ for the right-half arch, which is employed for the analytical solution since loading and geometry are symmetrical to the vertical axis that passes through the mid-span as shown in Fig. 4. Following the thin-walled shell theory, the displacement components are expressed into

$$v(z, \phi) = v_0(\phi) + \frac{z}{R}\frac{dw_0(\phi)}{d\phi} \tag{1}$$

$$w(z, \phi) = w_0(\phi) \tag{2}$$

where $v_0(\phi)$ and $w_0(\phi)$ are the tangential (circumferential) and radial displacements at the mid-surface of the arch, respectively. z is the distance from any point to the mid-surface in the radial direction. The

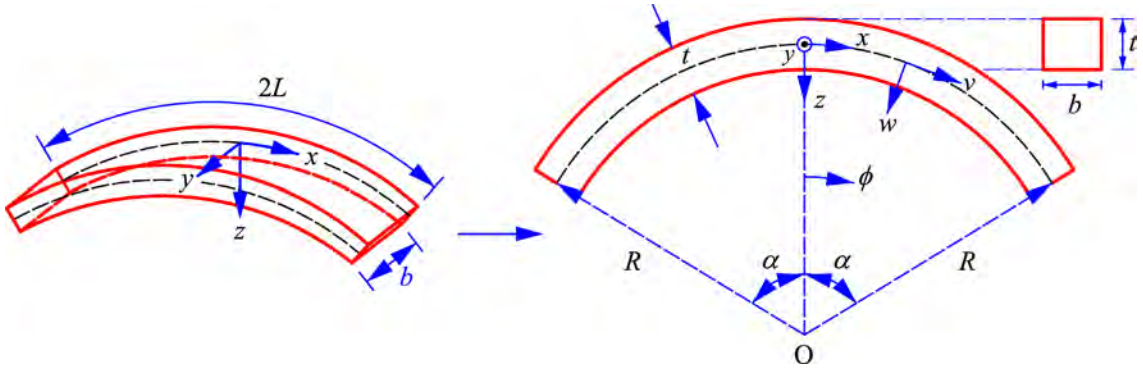

Fig. 4. Coordinate system and displacement definition of an FGM arch.

arch consists of two material mixtures as shown in Fig. 2. The volume fraction of ceramic V_c and metal fraction V_m take the form of [15,16,21,32]

$$V_c = \left(\frac{1}{2} - \frac{z}{t}\right)^n \quad \text{and} \quad V_m = 1 - V_c \tag{3}$$

where n ($n \geq 0$) is volume fraction exponent. Fig. 5 shows the effect of volume fraction exponent (n) on the fraction of ceramic (V_c). Following Voigt mixture theory, Young's modulus $E(z)$ and coefficient of thermal expansion $\lambda(z)$ vary in the thickness direction, yielding

$$E(z) = E_m + (E_c - E_m)\left(\frac{1}{2} - \frac{z}{t}\right)^n \tag{4a}$$

$$\lambda(z) = \lambda_m + (\lambda_c - \lambda_m)\left(\frac{1}{2} - \frac{z}{t}\right)^n \tag{4b}$$

where E_c (E_m) is Young's modulus of the ceramic (metal), and λ_c (λ_m) is the coefficient of thermal expansion of the ceramic (metal), respectively.

At any position of the arch wall, the total strain $\varepsilon(\phi)$ consists of two parts: one is the strain at the mid-axis $\varepsilon_0(\phi)$, and the other is the strain induced by bending curvature, $z\kappa$, respectively. Therefore, we have

$$\varepsilon(\phi) = \varepsilon_0(\phi) + z\kappa \tag{5a}$$

$$\varepsilon_0(\phi) = \frac{w_0(\phi)}{R} - \frac{1}{R}\frac{\partial v_0(\phi)}{\partial \phi} - \frac{1}{2R^2}\left[\frac{\partial w_0(\phi)}{\partial \phi}\right]^2 \tag{5b}$$

The temperature rise (ΔT) is introduced before the external pressure. The hoop strain induced by this thermal effect is

$$\varepsilon_T = \lambda(z)\Delta T \tag{6}$$

Similarly, the bending curvature is obtained from

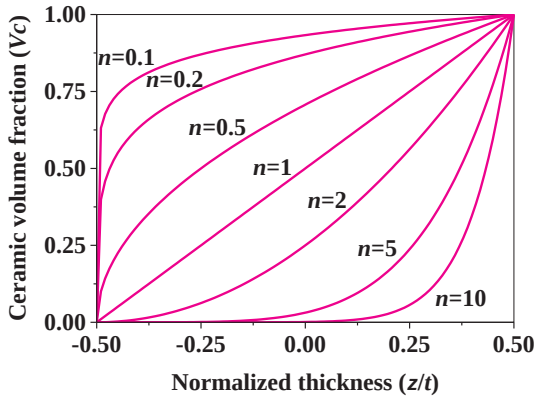

Fig. 5. Effects of volume fraction exponent (n) on the ceramic fractions (V_c).

$$\kappa = \frac{w_0(\phi)}{R^2} + \frac{1}{R^2}\frac{\partial^2 w_0(\phi)}{\partial \phi^2} \tag{7}$$

It is noted the underlined term in Eq. (5b) is the increase of strain at the neutral axis due to bending curvature [23,31,33]. Therefore, this term is the geometric nonlinear term and significantly affects the buckling pressure [34]. Based on the one-dimensional thermoelastic scheme, the hoop stress yields

$$\sigma(z, \phi) = E(z)[\varepsilon_0(\phi) + z\kappa + \varepsilon_T] \tag{8}$$

For the half arch, the total potential energy function is calculated by

$$\Pi = \frac{1}{2}\iiint_0^V E(z)[\varepsilon_0(\phi) + \varepsilon_T + z\kappa]^2 dV - W \tag{9}$$

where V is the volume of half arch, and W is the work done by external pressure. Therefore

$$W = Pb\int_0^L w_0(\phi) ds \tag{10}$$

where $s = R\phi$, and P is the pressure loading, respectively.

3. Determination of critical buckling pressure

When an FGM arch is in a thermal rise environment, an upward displacement occurs. In such a case, external pressure on the arch will result in deformations as shown in Fig. 6. Due to symmetrical deformations to line OC, only the right-half arch is examined. The radial displacement is assumed to be [22,26,29]

$$w_0(\phi) = \begin{cases} -(w_1 + w_2)\cos^2\frac{\pi\phi}{2\phi_0} + w_2;\ 0 \leq \phi \leq \phi_0 \\ w_2\cos^2\frac{\pi(\phi - \phi_0)}{2(\alpha - \phi_0)};\ \phi_0 \leq \phi \leq \alpha \end{cases} \quad \text{clampe}$$

$$\text{d} - \text{clamped ends} \tag{11a}$$

$$w_0(\phi) = \begin{cases} -(w_1 + w_2)\cos^2\frac{\pi\phi}{2\phi_0} + w_2;\ 0 \leq \phi \leq \phi_0 \\ w_2\cos\frac{\pi(\phi - \phi_0)}{2(\alpha - \phi_0)};\ \phi_0 \leq \phi \leq \alpha \end{cases} \quad \text{pinned} - \text{pinned ends} \tag{11b}$$

The rotation and bending curvature are calculated by taking the first and second derivatives of $w_0(\phi)$ to s, so we have

$$\frac{1}{R}\frac{\partial w_0(\phi)}{\partial \phi} = \begin{cases} \frac{(w_1 + w_2)\pi}{2R\phi_0}\sin\frac{\pi\phi}{\phi_0};\ 0 \leq \phi \leq \phi_0 \\ \frac{-w_2\pi}{2R(\alpha - \phi_0)}\sin\frac{\pi(\phi - \phi_0)}{(\alpha - \phi_0)};\ \phi_0 \leq \phi \leq \alpha \end{cases} \quad \text{clamped} - \text{clamped ends} \tag{11c}$$

$$\frac{1}{R}\frac{\partial w_0(\phi)}{\partial \phi} = \begin{cases} \frac{(w_1 + w_2)\pi}{2R\phi_0}\sin\frac{\pi\phi}{\phi_0};\ 0 \leq \phi \leq \phi_0 \\ \frac{-w_2\pi}{2R(\alpha - \phi_0)}\sin\frac{\pi(\phi - \phi_0)}{2(\alpha - \phi_0)};\ \phi_0 \leq \phi \leq \alpha \end{cases} \quad \text{pinned} - \text{pinned ends} \tag{11d}$$

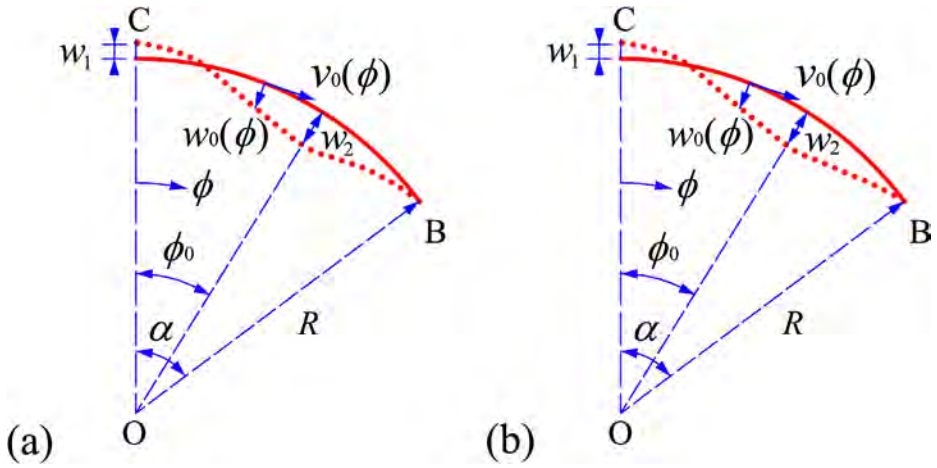

Fig. 6. Geometric parameters of half heated FGM arch under external pressure for (a) clamped-clamped, and (b) pinned-pinned arches.

$$\frac{1}{R^2}\frac{\partial^2 w_0(\phi)}{\partial\phi^2} = \begin{cases} \frac{(w_1+w_2)\pi^2}{2R^2\phi_0^2}cos\frac{\pi\phi}{\phi_0};\ 0\le\phi\le\phi_0 \\ \frac{-w_2\pi^2}{2R^2(\alpha-\phi_0)^2}cos\frac{\pi(\phi-\phi_0)}{(\alpha-\phi_0)};\ \phi_0\le\phi\le\alpha \end{cases} \quad \text{clampe}$$

$$\text{d}-\text{clamped ends} \tag{11e}$$

$$\frac{1}{R^2}\frac{\partial^2 w_0(\phi)}{\partial\phi^2} = \begin{cases} \frac{(w_1+w_2)\pi^2}{2R^2\phi_0^2}cos\frac{\pi\phi}{\phi_0};\ 0\le\phi\le\phi_0 \\ \frac{-w_2\pi^2}{4R^2(\alpha-\phi_0)^2}cos\frac{\pi(\phi-\phi_0)}{2(\alpha-\phi_0)};\ \phi_0\le\phi\le\alpha \end{cases}$$

$$\text{pinned}-\text{pinned ends} \tag{11f}$$

The curvature is continuous at $\phi=\phi_0$, so we get

$$w_1 = \begin{cases} \frac{-\gamma^2+2\gamma}{(\gamma-1)^2}w_2; & \text{clamped-clamped ends} \\ \frac{-2\gamma^2+4\gamma-1}{2(\gamma-1)^2}w_2; & \text{pinned-pinned ends} \end{cases} \tag{12}$$

where $\gamma=\alpha/\phi_0$. Here, the hoop strain is averaged through the arch span to obtain the equilibrium paths. Following the previous work [26–31], the averaged hoop strain $\bar{\varepsilon}$ yields

$$\bar{\varepsilon}\int_0^{R\alpha} ds = \int_0^{R\alpha}\left\{\frac{w_0(\phi)}{R}-\frac{1}{R}\frac{\partial v_0(\phi)}{\partial\phi}-\frac{1}{2R^2}\left[\frac{\partial w_0(\phi)}{\partial\phi}\right]^2\right\}ds \tag{13}$$

Noting that the following integration vanishes

$$\int_0^{R\alpha}\left[-\frac{1}{R}\frac{\partial v_0(\phi)}{\partial\phi}\right]ds = v_0(0)-v_0(\alpha)=0 \tag{14}$$

Since $v_0(0)=0$ at the crown and $v_0(\alpha)=0$ at the right ends for both clamped-clamped and pinned-pinned arches, respectively. With the introduction of Eqs. (11), (12) and (14) to Eq. (13), we obtain

$$\bar{\varepsilon} = \frac{w_2}{R}\tau_1 - \frac{w_2^2\pi^2}{16R^2\alpha^2}\tau_2 \tag{15a}$$

where

$$\tau_1 = \begin{cases} \frac{\gamma^2-\gamma-1}{2(\gamma-1)^2}; & \text{clamped-clamped ends} \\ \frac{1.273\gamma^3-1.819\gamma^2-0.181\gamma+0.227}{2\gamma(\gamma-1)^2}; & \text{pinned-pinned ends} \end{cases} \tag{15b}$$

$$\tau_2 = \begin{cases} \frac{\gamma^4-3\gamma^3+3\gamma^2}{(\gamma-1)^4}; & \text{clamped-clamped ends} \\ \frac{4\gamma^4-12\gamma^3+12\gamma^2-3\gamma}{4(\gamma-1)^4}; & \text{pinned-pinned ends} \end{cases} \tag{15c}$$

After substituting $\varepsilon_0(\phi)$ by $\bar{\varepsilon}$ in Eq. (9), the energy function Π is expressed into

$$\Pi = \begin{cases} \frac{R\alpha}{2E_1}\bar{N}^2+\frac{\Gamma_3 w_2^2\pi^4}{16R^3\alpha^3}\tau_3 - PRb\alpha w_2\tau_1; & \text{clamped-clamped ends} \\ \frac{R\alpha}{2E_1}\bar{N}^2+\frac{\Gamma_3 w_2^2\pi^4}{16R^3\alpha^3}\tau_3+\frac{\pi(\Gamma_2\bar{\varepsilon}+M_T)w_2\tau_4}{2R\alpha} - PRb\alpha w_2\tau_1; & \\ \text{pinned-pinned ends} & \end{cases} \tag{16}$$

where $\bar{N}$ is the averaged hoop force, and written by

$$\bar{N} = \Gamma_1\bar{\varepsilon}+N_T \tag{17a}$$

$$\tau_3 = \begin{cases} \frac{\gamma^4}{(\gamma-1)^4}; & \text{clamped-clamped ends} \\ \frac{\gamma^4}{4(\gamma-1)^4}; & \text{pinned-pinned ends} \end{cases} \tag{17b}$$

$$\tau_4 = \frac{\gamma}{(\gamma-1)} \tag{17c}$$

Here, Γ_1, Γ_2, Γ_3 are the stretching, stretching-bending and bending stiffness respectively, and N_T, M_T are the thermal hoop force and bending moment respectively, and take the form of

$$\Gamma_1 = b\int_{-t/2}^{t/2}E(z)dz = bt[E_m+(E_c-E_m)/(n+1)] \tag{18a}$$

$$\Gamma_2 = b\int_{-t/2}^{t/2}E(z)zdz = \frac{nbt^2(E_c-E_m)}{2(n+1)(n+2)} \tag{18b}$$

$$\Gamma_3 = b\int_{-t/2}^{t/2}E(z)z^2dz = \frac{bt^3}{12}\left[E_m+\frac{(3n^2+3n+6)}{(n+1)(n+2)(n+3)}(E_c-E_m)\right] \tag{18c}$$

$$N_T = b\int_{-t/2}^{t/2}E(z)\lambda(z)\Delta Tdz = bt\Delta T\left[E_m\lambda_m+\frac{E_m(\lambda_c-\lambda_m)+(E_c-E_m)\lambda_m}{(n+1)}+\frac{(E_c-E_m)(\lambda_c-\lambda_m)}{(2n+1)}\right] \tag{18d}$$

$$M_T = b\int_{-t/2}^{t/2}E(z)\lambda(z)\Delta Tzdz = nbt^2\Delta T\left[\frac{E_m(\lambda_c-\lambda_m)+(E_c-E_m)\lambda_m}{2(n+1)(n+2)}+\frac{(E_c-E_m)(\lambda_c-\lambda_m)}{(2n+1)(2n+2)}\right] \tag{18e}$$

3.1. Clamped-clamped ends arch

Two unknowns, w_2 and γ, exist in Eq. (16). For the clamped-clamped arch, the principle of minimum potential energy requires the first derivative of the total potential energy function $\delta\Pi=0$, and the

second derivative $\delta^2\Pi < 0$, yielding

$$\delta\Pi = \frac{\partial\Pi}{\partial w_2}\delta w_2 + \frac{\partial\Pi}{\partial\gamma}\delta\gamma = 0 \rightarrow \frac{\partial\Pi}{\partial w_2} = 0 \text{ and } \frac{\partial\Pi}{\partial\gamma} = 0 \tag{19a}$$

$$\delta^2\Pi < 0 \tag{19b}$$

The first derivative of the averaged hoop force yields

$$\frac{\partial\bar{N}}{\partial w_2} = \Gamma_1\left(\frac{1}{R}\tau_1 - \frac{2w_2\pi^2}{16R^2\alpha^2}\tau_2\right) \tag{20a}$$

$$\frac{\partial\bar{N}}{\partial\gamma} = \Gamma_1\left(\frac{w_2}{R}\frac{d\tau_1}{d\gamma} - \frac{w_2^2\pi^2}{16R^2\alpha^2}\frac{d\tau_2}{d\gamma}\right) \tag{20b}$$

Therefore, two nonlinear equilibrium equations are obtained from Eq. (19a), yielding

$$R\bar{N}\left(\frac{1}{R} - \frac{w_2\pi^2}{16R^2\alpha^2}\frac{2\tau_2}{\tau_1}\right) + \frac{\Gamma_3 w_2\pi^4}{16R^3\alpha^4}\frac{2\tau_3}{\tau_1} = PRb \tag{21a}$$

$$R\bar{N}\left(\frac{1}{R} - \frac{w_2\pi^2}{16R^2\alpha^2}\frac{d\tau_2}{d\gamma}/\frac{d\tau_1}{d\gamma}\right) + \frac{\Gamma_3 w_2\pi^4}{16R^3\alpha^4}\frac{d\tau_3}{d\gamma}/\frac{d\tau_1}{d\gamma} = PRb \tag{21b}$$

Substituting Eqs. (21a) into (21b) to eliminate the term PRb, the averaged hoop force takes an alternative form of

$$\bar{N} = \frac{\Gamma_3\pi^2}{R^2\alpha^2}\Phi_1 \tag{22a}$$

where

$$\Phi_1 = \left(\frac{2\tau_3}{\tau_1} - \frac{d\tau_3}{d\gamma}/\frac{d\tau_1}{d\gamma}\right)/\left(\frac{2\tau_2}{\tau_1} - \frac{d\tau_2}{d\gamma}/\frac{d\tau_1}{d\gamma}\right) \tag{22b}$$

Introducing Eq. (17a) to Eq. (22a), a quadratic equation is obtained in terms of w_2, yielding

$$\frac{\tau_2\pi^2}{16R^2\alpha^2}w_2^2 - \frac{\tau_1}{R}w_2 + \frac{\Gamma_3\pi^2\Phi_1}{\Gamma_1R^2\alpha^2} - \frac{N_T}{\Gamma_1} = 0 \tag{23}$$

Solving Eq. (23) yields two positive roots

$$w_2 = \frac{8\tau_1R\alpha^2}{\tau_2\pi^2}\left[1 \pm \sqrt{1 - \frac{\tau_2\pi^2}{4\tau_1^2\alpha^2}\left(\frac{\Gamma_3\pi^2\Phi_1}{\Gamma_1R^2\alpha^2} - \frac{N_T}{\Gamma_1}\right)}\right] \tag{24}$$

and only the smaller positive one satisfies Eq. (19b). By substituting Eq. (24) into Eq. (12), the crown displacement can be calculated as

$$w_1 = \frac{8\tau_1R\alpha^2}{\tau_2\pi^2}\frac{(-\gamma^2+2\gamma)}{(\gamma-1)^2}\left[1 \pm \sqrt{1 - \frac{\tau_2\pi^2}{4\tau_1^2\alpha^2}\left(\frac{\Gamma_3\pi^2\Phi_1}{\Gamma_1R^2\alpha^2} - \frac{N_T}{\Gamma_1}\right)}\right] \tag{25}$$

Introducing Eq. (22a) into Eq. (21a), the pressure is in the form of

$$P = \frac{\Gamma_3\pi^2}{bR^3\alpha^2}\Phi_1 + \frac{\Gamma_3\pi^4(\tau_3 - \tau_2\Phi_1)}{8bR^4\alpha^4\tau_1}w_2 \tag{26}$$

Then introducing Eq. (24) to Eq. (26) to eliminate w_2, the pressure is obtained as

$$P = \frac{\Gamma_3\pi^2}{bR^3\alpha^2}\left[\left(\frac{\tau_3}{\tau_2}\right) \pm \left(\frac{\tau_3}{\tau_2} - \Phi_1\right)\sqrt{1 - \frac{\tau_2\pi^2}{4\tau_1^2\alpha^2}\left(\frac{\Gamma_3\pi^2\Phi_1}{\Gamma_1R^2\alpha^2} - \frac{N_T}{\Gamma_1}\right)}\right] \tag{27}$$

To identify the practical equilibrium path, it is necessary to take the first derivative of P to γ, yielding

$$\frac{\partial P}{\partial\gamma} = 0 \tag{28}$$

Newton-Raphson iteration will be used to obtain γ_{cr} in Eq. (28). The specific iteration is as follows: defining an initial γ_0, then substituting γ_0 into Eq. (28), if $\left|\frac{\partial P}{\partial\gamma}\right| \geq 0.0001$, then define $\gamma_1 = \gamma_0 - 0.001$, if $\left|\frac{\partial P}{\partial\gamma}\right| \geq 0.0001$, then define $\gamma_2 = \gamma_1 - 0.001$…repeating the above process until to find $\left|\frac{\partial P}{\partial\gamma}\right| < 0.0001$ and its corresponding γ_{cr}. With the substitution of γ_{cr} into Eq. (27), the critical buckling pressure for the clamped-clamped arches is

$$P_{cr} = \frac{\Gamma_3\pi^2}{bR^3\alpha^2}\left[\left(\frac{\tau_{3cr}}{\tau_{2cr}}\right) \pm \left(\frac{\tau_{3cr}}{\tau_{2cr}} - \Phi_{1cr}\right)\sqrt{1 - \frac{\tau_{2cr}\pi^2}{4\tau_{1cr}^2\alpha^2}\left(\frac{\Gamma_3\pi^2\Phi_{1cr}}{\Gamma_1R^2\alpha^2} - \frac{N_T}{\Gamma_1}\right)}\right] \tag{29}$$

where τ_{1cr}, τ_{2cr}, τ_{3cr} and Φ_{1cr} correspond to $\gamma = \gamma_{cr}$.

3.2. Pinned-pinned ends arch

Taking the first derivative of the energy function Eq. (16) for the pinned-pinned case to the two unknowns w_2 and γ, the two equilibrium equations in Eq. (21) are revised into

$$\left(1 - \frac{w_2\pi^2}{16R\alpha^2}\frac{2\tau_2}{\tau_1}\right)\bar{N} + \frac{\pi}{2R\alpha^2}\frac{\tau_4}{\tau_1}\left[(\Gamma_2\bar{\varepsilon} + M_T) + \Gamma_2 w_2\frac{\partial\bar{\varepsilon}}{\partial w_2}\right] + \frac{\Gamma_3 w_2\pi^4}{16R^3\alpha^4}\frac{2\tau_3}{\tau_1} = PRb \tag{30a}$$

$$\left(1 - \frac{w_2\pi^2}{16R\alpha^2}\frac{d\tau_2}{d\gamma}/\frac{d\tau_1}{d\gamma}\right)\bar{N} + \frac{\pi}{2R\alpha^2}\left[(\Gamma_2\bar{\varepsilon} + M_T)\frac{d\tau_4}{d\gamma} + \Gamma_2\tau_4\frac{\partial\bar{\varepsilon}}{\partial\gamma}\right]/\frac{d\tau_1}{d\gamma} + \frac{\Gamma_3 w_2\pi^4}{16R^3\alpha^4}\frac{d\tau_3}{d\gamma}/\frac{d\tau_1}{d\gamma} = PRb \tag{30b}$$

Substituting Eq. (30a) into (30b), we get a cubic formula in terms of w_2, yielding

$$\frac{\pi^2}{16R^2\alpha^2}w_2^3 - \left[\frac{\tau_1}{R} + \frac{\pi\Gamma_2\Phi_2}{2R^2\alpha^2\Gamma_1\tau_2}\left(\frac{\tau_4}{\Phi_2} + 1\right)\right]w_2^2 + \left(\frac{\Gamma_3\pi^2\Phi_1}{\Gamma_1R^2\tau_2\alpha^2} + \frac{8\Gamma_2\tau_1\Phi_2}{\Gamma_1R\tau_2\pi} - \frac{N_T}{\Gamma_1\tau_2}\right)w_2 + \frac{8\Phi_2M_T}{\Gamma_1\tau_2\pi} = 0 \tag{31}$$

where

$$\Phi_2 = \left(\frac{\tau_4}{\tau_1} - \frac{d\tau_4}{d\gamma}/\frac{d\tau_1}{d\gamma}\right)/\left(\frac{2\tau_2}{\tau_1} - \frac{d\tau_2}{d\gamma}/\frac{d\tau_1}{d\gamma}\right) \tag{32}$$

For a given value of γ, we get three roots of w_{2cr} in Eq. (31), and only the minimum positive root, w_{2cr} satisfies Eq. (19b). With the Newton-Raphson iteration algorithm, the critical γ_{cr} is obtained in Eq. (31). Then substituting w_{2cr} and γ_{cr} in Eq. (30a), the buckling pressure is calculated as

$$\begin{aligned} P_{cr} = {} & \frac{\Gamma_1}{b}\frac{w_{2cr}}{R^2\tau_{1cr}}\left(1 - \frac{3w_{2cr}\pi^2}{16R\alpha^2}\frac{\tau_{2cr}}{\tau_{1cr}} + \frac{w_{2cr}^2\pi^4}{128R^2\alpha^4}\frac{\tau_{2cr}^2}{\tau_{1cr}^2}\right) + \frac{N_T}{b} \\ & \left(\frac{1}{R} - \frac{w_{2cr}\pi^2}{8R^2\alpha^2}\frac{\tau_{2cr}}{\tau_1 cr}\right) + \frac{\Gamma_2}{b}\frac{\pi}{\alpha^2}\frac{\tau_{4cr}}{\tau_{1cr}} \\ & \left(\frac{w_{2cr}\tau_{1cr}}{R^3} - \frac{3w_{2cr}^2\pi^2\tau_{2cr}}{32R^4\alpha^2} + \frac{M_T}{2R^2\Gamma_2}\right) + \frac{\Gamma_3}{b}\frac{w_{2cr}\pi^4}{8R^4\alpha^4}\frac{\tau_{3cr}}{\tau_{1cr}} \end{aligned} \tag{33}$$

where τ_{1cr}, τ_{2cr}, τ_{3cr} and τ_{4cr} correspond to $\gamma = \gamma_{cr}$. Noting that the pressure capacity (P_{cr}) is independent of the arch width (b) after substituting Eq. (18) into Eq. (33). Accordingly, the unity width ($b = 1$) and plane stress condition are employed to improve the computational efficiency in the following numerical simulations.

4. Numerical analysis

4.1. Definition of the numerical model

The instability mechanism of the heated FGM arches under uniform pressure is evaluated by the software ABAQUS [35]. Following Refs. [36,37], the ceramic material of the outside layer is Silicon Nitride (Si_3N_4) and the metal material of the inside layer is Stainless steel (SUS304), respectively. The material properties can be expressed

Table 1
Material properties of SUS304 and Si_3N_4.

Material	Properties	Λ_{-1}	Λ_0	Λ_1	Λ_2	Λ_3
SUS304	$\lambda_m(K^{-1})$	0	12.33×10^{-6}	8.086×10^{-4}	0	0
	$E_m(Pa)$	0	210.04×10^{9}	3.079×10^{-4}	-6.534×10^{-7}	0
Si_3N_4	$\lambda_c(K^{-1})$	0	5.8723×10^{-6}	9.095×10^{-4}	0	0
	$E_c(Pa)$	0	348.43×10^{9}	-3.07×10^{-4}	2.16×10^{-7}	-8.946×10^{-11}

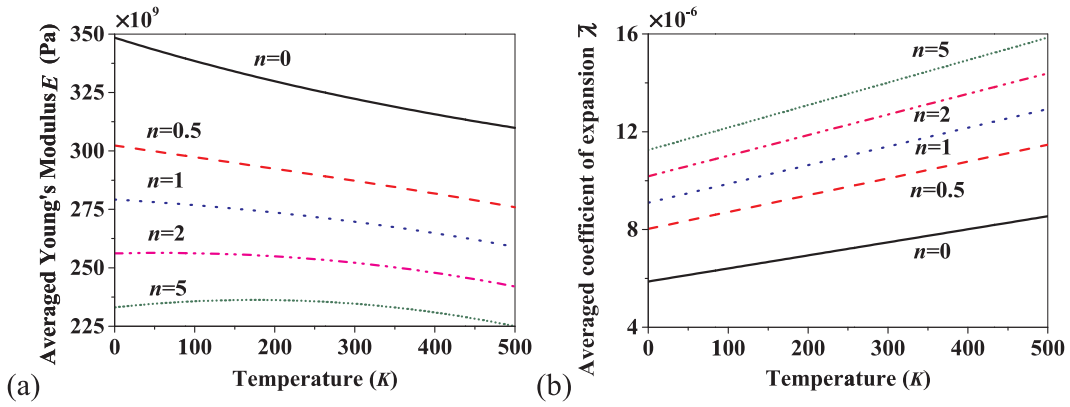

Fig. 7. The variation of averaged Young's Modulus and coefficient of thermal expansion with temperature.

quantitatively into

$$\Lambda = \Lambda_0(\Lambda_{-1}T^{-1} + 1 + \Lambda_1 T + \Lambda_2 T^2 + \Lambda_3 T^3) \tag{34}$$

where Λ_{-1}, Λ_0, Λ_1, Λ_2 and Λ_3 are constant as shown in Table 1. Here, the averaged Young's modulus ($\bar{E}$), as well as the coefficient of thermal expansion ($\bar{\lambda}$) are integrated as

$$\bar{E} = \int_{-t/2}^{t/2} bE(z)dz / \int_{-t/2}^{t/2} bdz = [E_m + (E_c - E_m)/(n+1)] \tag{35a}$$

$$\bar{\lambda} = \int_{-t/2}^{t/2} b\lambda(z)dz / \int_{-t/2}^{t/2} bdz = [\lambda_m + (\lambda_c - \lambda_m)/(n+1)] \tag{35b}$$

and plotted in Fig. 7. One may state that $\bar{\lambda}$ is linear with temperature when n increases from 0 to 5. On the other hand, $\bar{E}$ reduces with temperature except for the case $n = 5$, where $\bar{E}$ increases first to a maximum level at $T = 235.6K$, and then decreases with the temperature rise. It is easy to implement the definition of Young's modulus and coefficient of thermal expansion by turning on the switch "use temperature dependent data" in Property module. Poisson's ratio is 0.28 for simplicity [36].

The geometric parameter is defined as: the radius $R = 1$m and the thickness $t = 0.005$m, so we get $R/t = 200$. For the shallow arch, the central angle α varies from $\pi/12$ to $\pi/4$. In the thickness direction, the arch is divided evenly into twenty layers ($N = 20$). The material properties are the same in each layer and varies from one layer to another. The effect of layer number on the buckling pressure will be examined later. The arch is discrete with 9600 *CPS8R* elements for the case $R/t = 200$ and $\alpha = \pi/12$ as shown in Fig. 8(a), where *CPS8R* represents eight-node reduced-integration plane stress elements. For the clamped-clamped arch, the two ends are fixed without any displacements or rotations. For the pinned-pinned arch, the two ends rotate freely as shown in Fig. 8(b). The ambient temperature field (i.e. $T_{amb} = 293.15\ K$) and the expected temperature T are defined in the first step and the second step of the Abaqus model. Therefore, the temperature rise ($\Delta T = T - T_{amb}$) generates. After that, the uniform pressure is applied at the outside surface as shown in Fig. 8(b).

In addition, the geometric nonlinearities are introduced by switching on the Nlgeom (Non-linear-geometry) option in the Step module of the numerical model. The modified arc-length algorithm is taken to trace the load-displacement path [38–40] since large displacements or rotations may occur in the present simulation. Only four parameters are defined, including the initial, minimum, maximum increments, and the initial reference loading in the first step. The subsequent pressure value and the displacement size are calculated automatically to track the whole equilibrium paths in the following steps.

4.2. Comparisons and discussions

The numerical results are compared with the analytical solutions of Eq. (29) for clamped-clamped arches and Eq. (33) for pinned-pinned arches as shown in Table 2. One may observe the numerical buckling pressure are in good agreement with the analytical solutions, and the maximum difference is no more than 5% for all examined cases with two temperature rises (ΔT), four different central angles (α) and five different volume fraction exponents (n), respectively. Moreover, a higher value of volume fraction exponent results in a lower critical buckling pressure except for a few pinned-pinned cases with $n = 5$ and $\Delta T = 400K$. This is because a higher thermal displacement (w_T in Fig. 3(a)) generates due to the more non-symmetrical distribution of the material properties to the mid-surface of the pinned-pinned arch with $n = 5$ when $\Delta T = 400K$. Such displacement (w_T) contributes more to the critical buckling pressure than the effects of the modulus reduction induced by temperature rise.

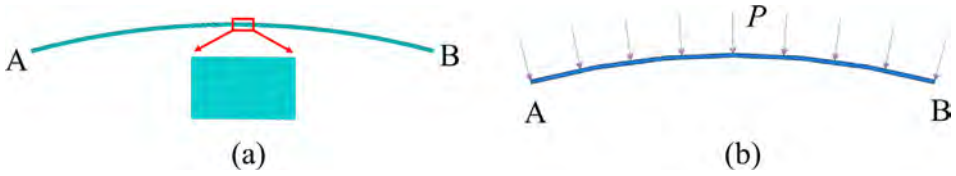

Fig. 8. (a) Mesh, and (b) boundaries of a typical FGM arch.

Table 2
The comparison of critical buckling pressure between present analytical and numerical results.

ΔT	α	n	Clamped-clamped (MPa) difference			Pinned-pinned (MPa) difference		
			FEM (P_e)	Eq. (28) (P_a)	$\left\|\frac{P_a-P_e}{P_a}\right\|$	FEM (P_e)	Eq. (32) (P_a)	$\left\|\frac{P_a-P_e}{P_a}\right\|$
200	$\pi/12$	0	1.97	1.98	0.00	1.084	1.100	0.01
		0.5	1.74	1.74	0.00	0.862	0.886	0.03
		1	1.65	1.66	0.00	0.800	0.830	0.04
		2	1.59	1.59	0.00	0.772	0.798	0.03
		5	1.54	1.52	0.01	0.772	0.784	0.02
	$5\pi/36$	0	0.711	0.711	0.00	0.383	0.392	0.02
		0.5	0.623	0.622	0.00	0.297	0.308	0.03
		1	0.591	0.591	0.00	0.276	0.286	0.04
		2	0.568	0.567	0.00	0.266	0.275	0.03
		5	0.546	0.540	0.01	0.262	0.269	0.02
	$7\pi/36$	0	0.367	0.362	0.02	0.193	0.199	0.03
		0.5	0.321	0.316	0.02	0.151	0.155	0.03
		1	0.305	0.300	0.01	0.139	0.144	0.04
		2	0.292	0.288	0.02	0.133	0.138	0.04
		5	0.281	0.274	0.03	0.132	0.135	0.02
	$\pi/4$	0	0.228	0.219	0.04	0.116	0.120	0.04
		0.5	0.199	0.191	0.05	0.0913	0.0938	0.03
		1	0.188	0.181	0.04	0.0829	0.0868	0.05
		2	0.182	0.174	0.05	0.0799	0.0828	0.04
		5	0.174	0.165	0.05	0.0791	0.0815	0.03
400	$\pi/12$	0	1.99	2.06	0.03	1.115	1.154	0.03
		0.5	1.74	1.78	0.02	0.794	0.839	0.05
		1	1.65	1.68	0.02	0.728	0.764	0.05
		2	1.59	1.60	0.01	0.692	0.730	0.05
		5	1.53	1.52	0.01	0.709	0.731	0.03
	$5\pi/36$	0	0.701	0.726	0.03	0.383	0.402	0.05
		0.5	0.607	0.619	0.02	0.263	0.278	0.05
		1	0.571	0.582	0.02	0.237	0.249	0.05
		2	0.546	0.554	0.01	0.225	0.236	0.05
		5	0.523	0.521	0.00	0.227	0.236	0.04
	$7\pi/36$	0	0.359	0.367	0.02	0.193	0.203	0.05
		0.5	0.310	0.312	0.01	0.129	0.136	0.05
		1	0.291	0.293	0.01	0.117	0.123	0.05
		2	0.278	0.278	0.00	0.109	0.115	0.05
		5	0.266	0.262	0.02	0.110	0.116	0.05
	$\pi/4$	0	0.222	0.221	0.00	0.116	0.121	0.04
		0.5	0.192	0.188	0.02	0.0780	0.0824	0.05
		1	0.180	0.176	0.02	0.0696	0.0735	0.05
		2	0.173	0.167	0.03	0.0658	0.0693	0.05
		5	0.164	0.157	0.04	0.0668	0.0694	0.04

Fig. 9 emphasizes the effects of layer number (N) on the pressure capacity (buckling pressure). The central angle $\alpha = \pi/12$ and aspect ratio $R/t = 200$. For both boundary conditions examined, the variation of the buckling pressure is negligible when $N \geq 20$. Therefore, $N = 20$ is recommended in industrial manufacturing of the thin-walled FGM structures.

Figs. 10 and 11 depict the comparison of analytical and numerical pressure-displacement equilibrium curves. For clamped-clamped arches, the analytical equilibrium curves are obtained by combining $w_1 = w_1(\gamma)$ in Eq. (25) and $P = P(\gamma)$ in Eq. (27), while for pinned-pinned arches, the curves are obtained by combining $w_2 = w_2(\gamma)$ in Eq. (31) and $P = P(\gamma)$ in Eq. (33), respectively. Noting the crown displacement $w_1(\gamma)$ can be calculated by substituting the root of Eq. (31) into Eq. (12) for the pinned-pinned arches. For comparison, the corresponding numerical equilibrium paths are also replotted in Figs. 10 and 11, respectively. These numerical equilibrium paths show multiple maximum and minimum pressure, which will be explained later in next section. For the two boundary cases, the analytical equilibrium paths agree well with the numerical equilibrium paths both in pre- and post-buckling stages. However, the analytical equilibrium curves only obtain their paths from $a \rightarrow b \rightarrow c$, after point c, the equilibrium paths are unavailable from the analytical solution. This is because the displacement function of Eq. (11) is based on the symmetrical snap-through buckling deformation, and other deformations are not considered in Eq. (11). In fact, the equilibrium paths $a \rightarrow b \rightarrow c$ in Figs. 10 and 11 are enough since the post-buckling stages after point b are unstable and may be avoided in engineering applications.

To verify the validity and consistency of the present analytical and numerical results, a comparison study is performed with the result obtained by Pi and Bradford [22] for the homogeneous arch ($n = 0$) under external pressure and temperature loading. The arch material is ceramic, and the material properties depends on Eq. (33) with Young's modulus $E_c = 348,430\text{MPa}$, and coefficient of thermal expansion $\lambda_c = 5.8723 \times 10^{-6}K^{-1}$ when $T = 0$. The temperature increases from the ambient temperature T_{amb} to T, where $T_{amb} = 293.15K$, and $T = 493.15K$ and $693.15K$, respectively. The buckling pressure of the present analytical and numerical results, as well as the prediction proposed by Pi and Bradford [22], are depicted in Fig. 12. For two temperature rises $\Delta T = 200K$ and $400K$, the present analytical and numerical results are in good accordance with the prediction from Pi and Bradford [22] for both clamped-clamped and pinned-pinned arches. Therefore, the present numerical results are accurate and reliable to take the parametric study in the next section.

4.3. Parametric evaluations

Some parameters are evaluated and the numerical results are depicted in Figs. 13–28. Unless otherwise mentioned, the central angle $\alpha = \pi/12$, and the aspect ratio $R/t = 200$. The ambient temperature is $T_{amb} = 293.15K$. Figs. 13 and 14 depict the effects of volume fraction exponent ($n = 0, 0.5, 2, 5$) on the pressure capacity when $\Delta T = 200K$. The pressure capacity decreases with the increase of volume fraction exponent (n). This is because Young's modulus reduces when n

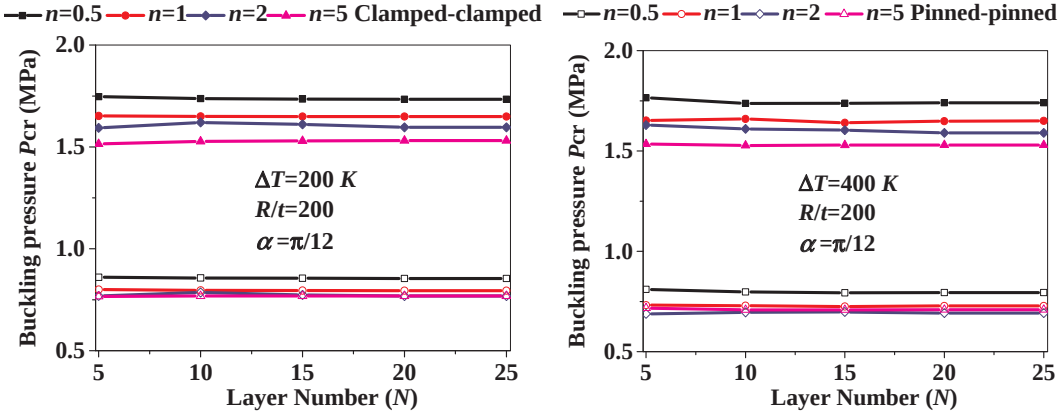

Fig. 9. Effect of layer number (N) on the pressure capacity of the FGM arches.

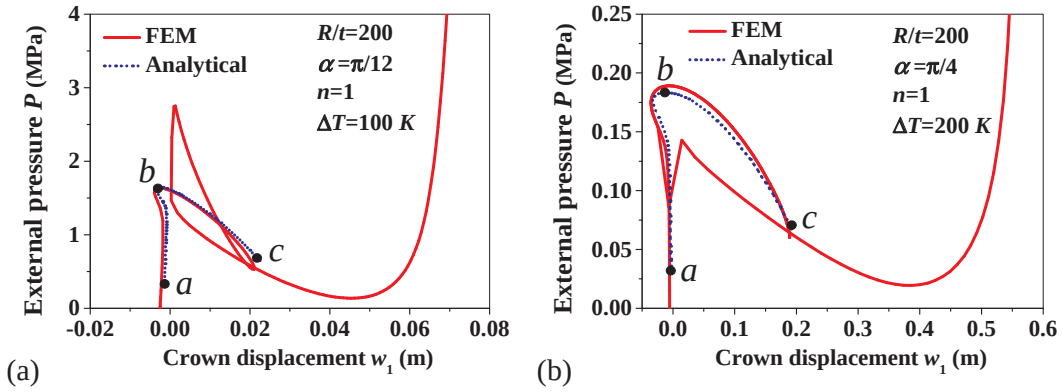

Fig. 10. Comparisons of equilibrium paths between analytical and numerical results for clamped-clamped arches.

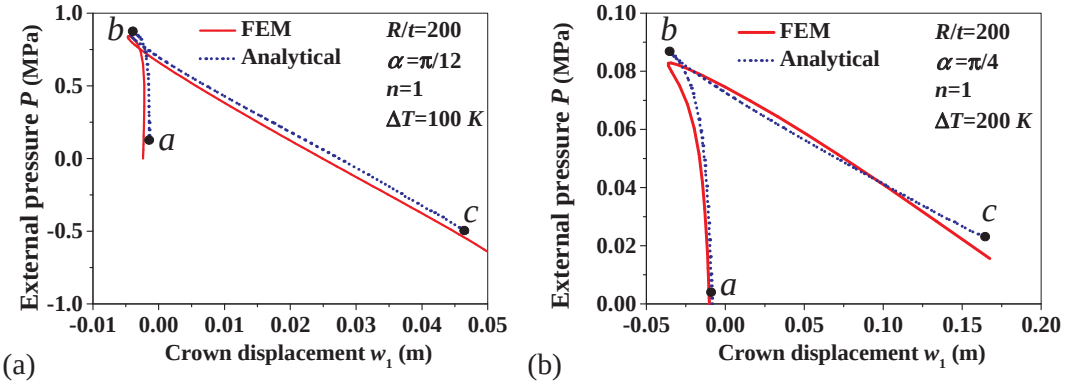

Fig. 11. Comparisons of equilibrium paths between analytical and numerical results for pinned-pinned arches.

increases as shown in Eq. (35a). Multiple equilibrium paths are observed for both clamped-clamped and pinned-pinned arches, respectively. Similar to the multiple equilibrium paths observed in the homogeneous arch as reported in Ref. [41], the FGM arch also shows equilibrium paths. For example, one typical multiple equilibrium path consists of three upper pressure limit (the maximum pressure) points, two lower pressure limit (the minimum pressure) points, and three displacement limit (the maximum and minimum displacements) points respectively, as shown in Fig. 13(a). The arch reaches its first buckling at point *b,* beyond which, the arch shows its unstable post-buckling behavior with large deformations. Therefore, the stages after point *b* are meaningless and may be avoided in engineering applications.

The equilibrium paths with different temperature rises ($\Delta T = 100K, 200K, 300K, 400K$) are plotted in Figs. 15 and 16 for both clamped-clamped and pinned-pinned arches, respectively. In all cases, the displacement starts from a negative value in the horizontal axis due to the thermal radially-outward displacement. Furthermore, the buckling pressure of the clamped-clamped arches in Fig. 15 is much higher than that in Fig. 16 for pinned-pinned arches, indicating the boundary condition exhibits a significant effect on the buckling pressure. In addition, the buckling pressure varies slightly with the temperature rise because the temperature rise shows two effects on the arch: on one hand, the temperature rise increases the radially-outward displacement, which is beneficial to the buckling pressure; on the other hand, the temperature rise reduces Young's modulus, which is unbeneficial to the buckling pressure. Therefore, the buckling pressure may be nonlinear with the temperature rise.

Figs. 17 and 18 show the distributions of bending moment through the arch span for clamped-clamped and pinned-pinned arches, respectively. All the values correspond to the critical buckling stage. For both

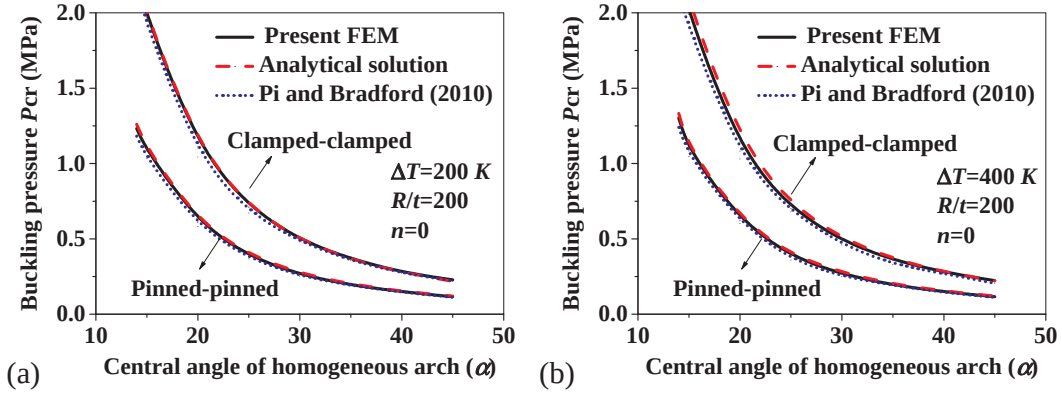

Fig. 12. Comparisons of buckling pressure between the present analytical and numerical results, as well as prediction from Pi and Bradford [22] for (a) $\Delta T = 200K$ and (b) $\Delta T = 400K$.

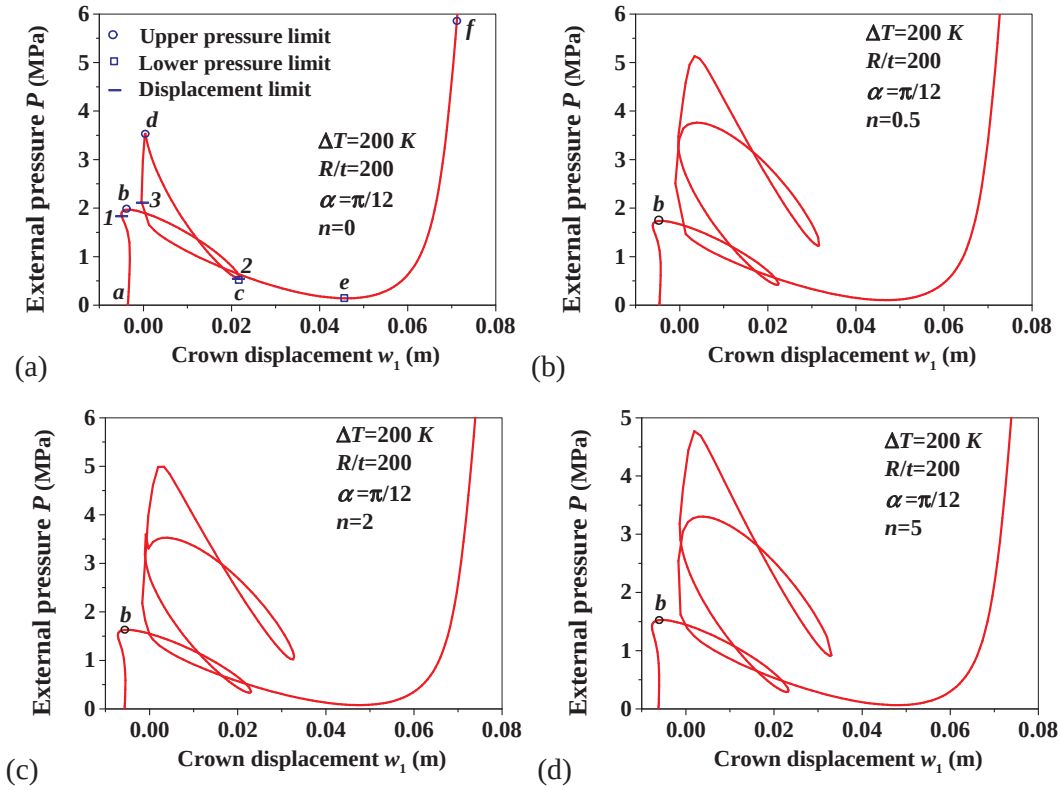

Fig. 13. The equilibrium paths of clamped-clamped FGM arches with different volume fraction exponents (n).

boundary conditions, the maximum positive bending moment occurs on the crown (mid-span), while the maximum negative bending moment occurs on the position between mid-span and edge, corresponding to the position with the maximum radial displacement. Furthermore, a higher temperature rise results in an increase in the bending moment. In addition, the bending moment is nonlinear with respect to volume fraction exponent (n). This is because the thermal moment generates due to the non-symmetrical distribution of material properties in the

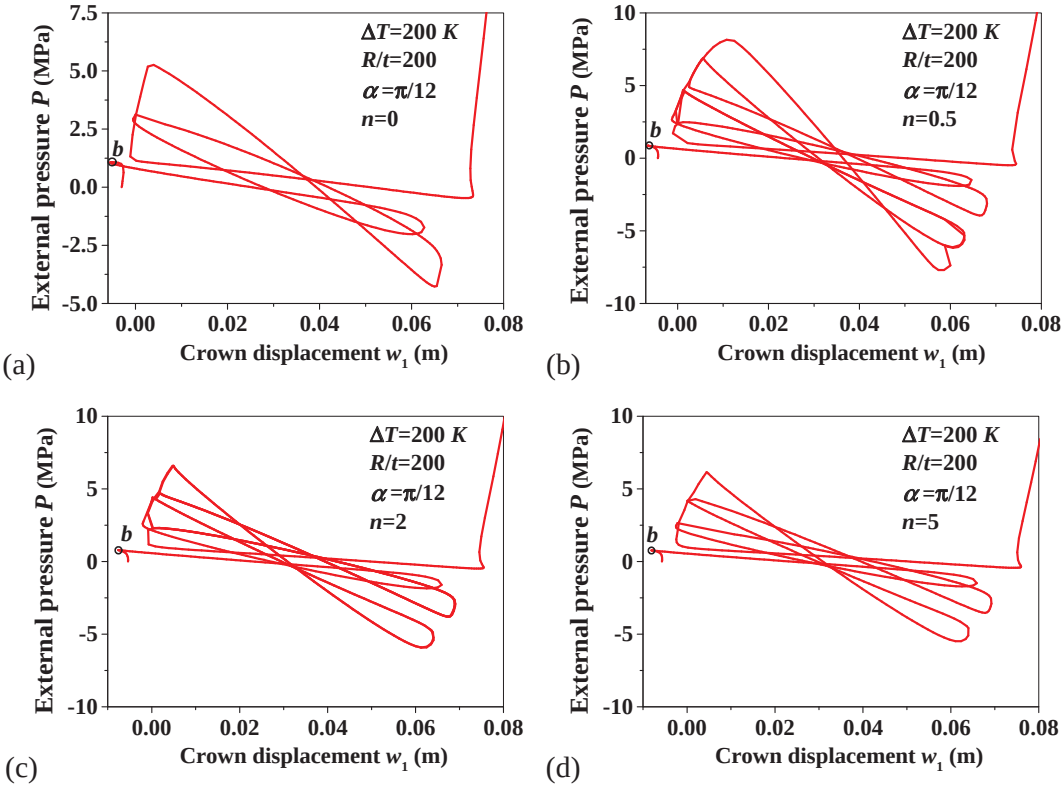

Fig. 14. The equilibrium paths of pinned-pinned FGM arches with different volume fraction exponents (n).

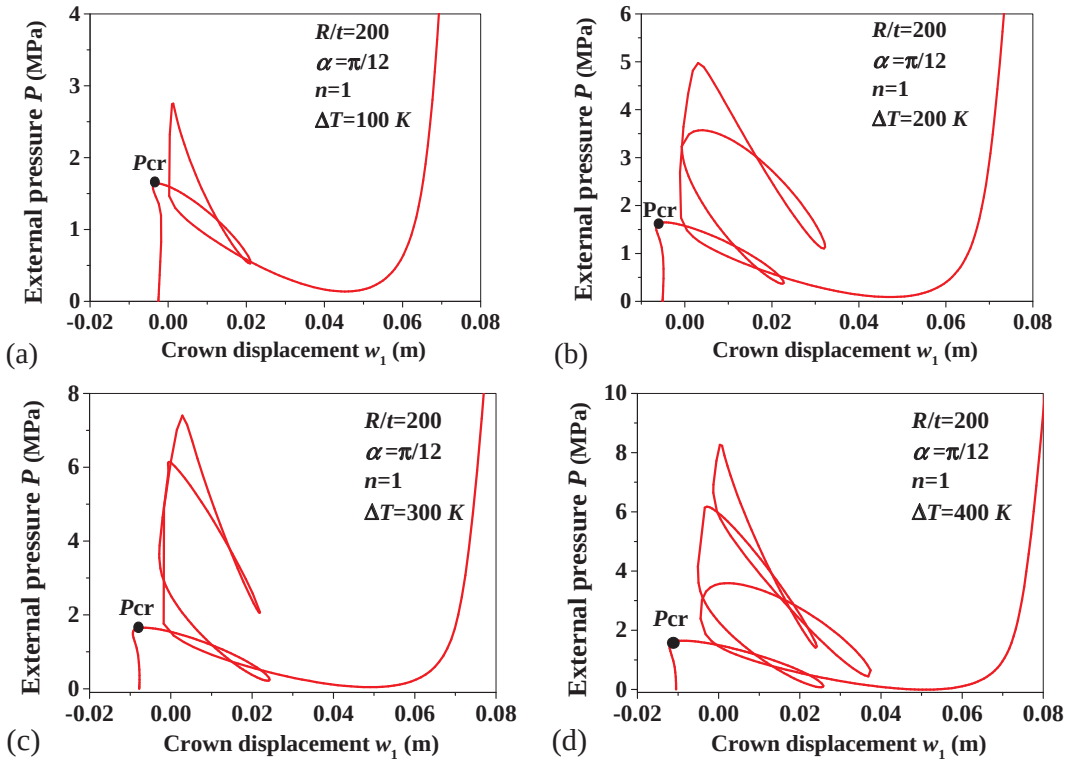

Fig. 15. The equilibrium paths of clamped-clamped FGM arches under varied temperature rises.

cross-section of the arch. From Eq. (18e), the thermal moment does not vary uniformly with volume fraction exponent. However, the difference of the bending moment is very small when volume fraction exponent varies from 0.5 to 5, for both clamped-clamped and pinned-pinned arches, respectively.

The distributions of the hoop force through the arch span are shown in Figs. 19 and 20 for clamped-clamped and pinned-pinned arches, respectively. All the values correspond to the critical buckling level. The

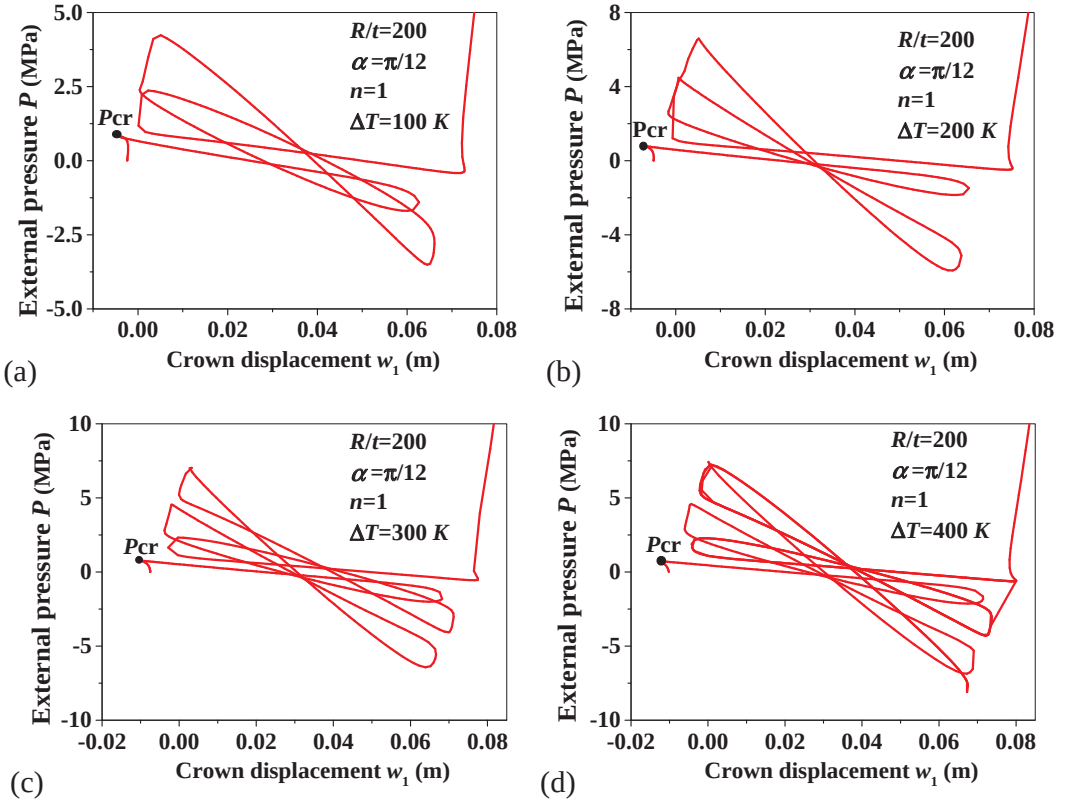

Fig. 16. The equilibrium paths of pinned-pinned FGM arches under varied temperature rises.

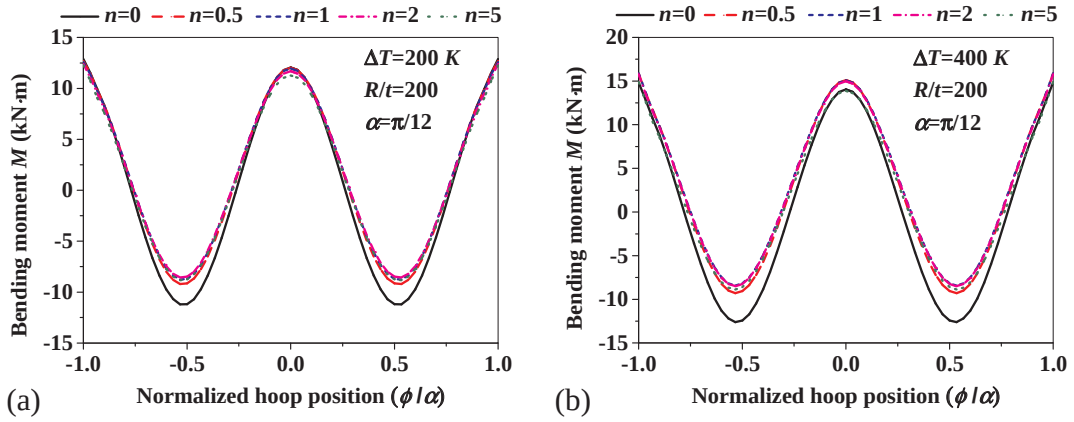

Fig. 17. The bending moment of the clamped-clamped arch with different temperature rises.

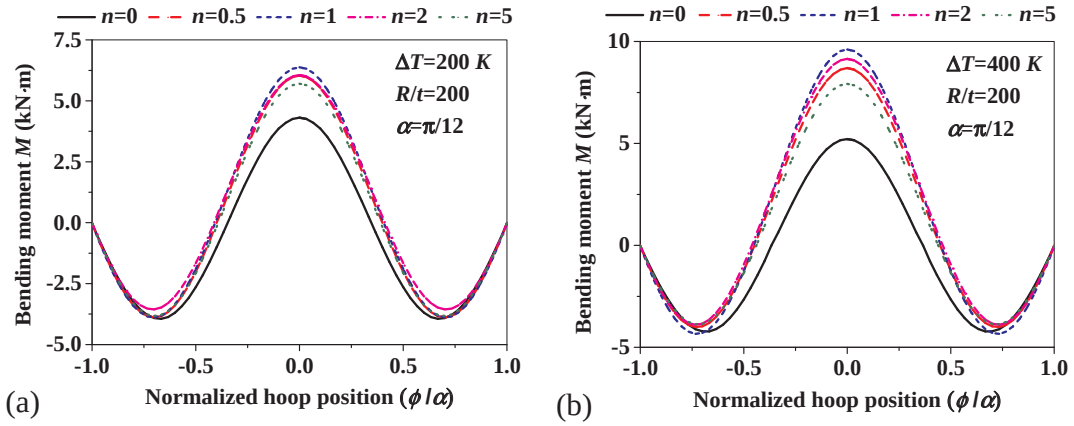

Fig. 18. The bending moment of the pinned-pinned arch with different temperature rises.

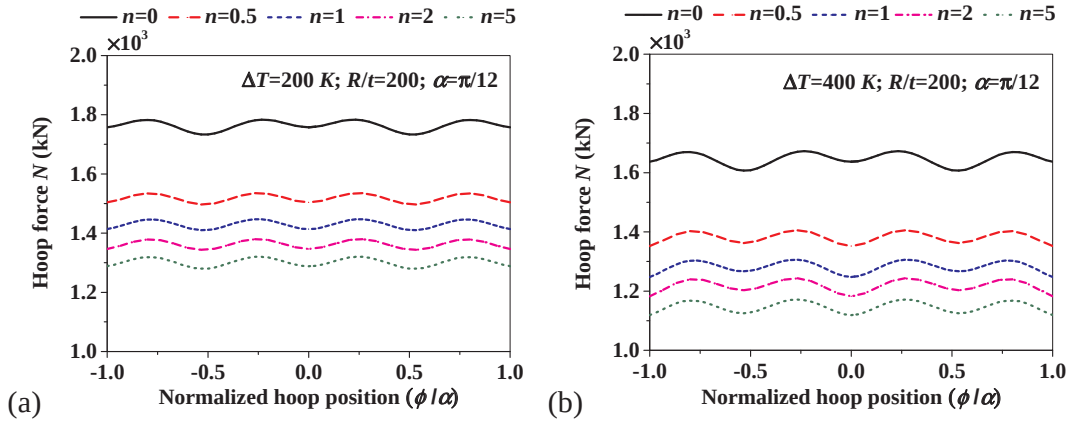

Fig. 19. The hoop force of the clamped-clamped arch with different temperature rises.

hoop force decreases with the increase of volume fraction exponent (n), and a higher temperature rise results in a lower hoop force. This is because the increase of volume fraction exponent and temperature rise will reduce Young's modulus. A few fluctuations of the hoop force are observed, and these fluctuations are neglected in Eq. (17). The hoop force is simplified as constant. Such a simplification results in an insignificant difference on the buckling pressure as shown in Table 2.

Figs. 21–23 depict the distribution of the hoop strain and stress at the top, bottom and middle surfaces through the span of the clamped-clamped arch. At the top surface, the strain and stress are positive near the crown area ($\phi/\alpha = 0$) whereas the hoop strain and stress are negative near the area with the maximum radial displacement as shown in Fig. 21(a) and (b). These features indicate that tension occurs at the top surface of the crown areas, while compression occurs at the top surface of the area with the maximum radial displacement. The top surface tensile strain on the crown area increases with increasing volume fraction exponent and temperature. However, the compressive stress and strain near the maximum displacement change slightly when the temperature rise increases from $200K$ to $400K$. On the other hand, the strain and stress at the bottom surface are negative near the crown area ($\phi/\alpha = 0$) whereas the hoop strain and stress are positive near the position with the maximum radial displacement as shown in Fig. 22. The bottom surface tensile strain on the maximum radial displacement area increases with increasing volume fraction exponent and temperature.

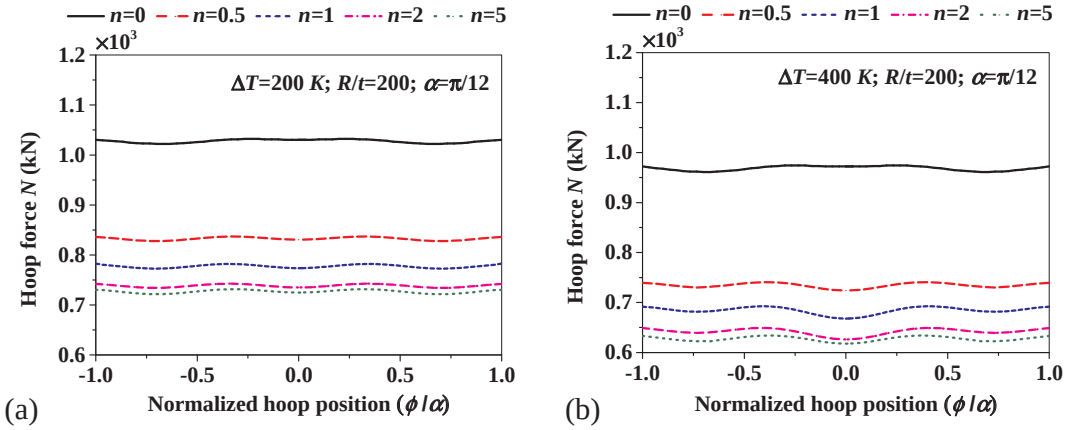

Fig. 20. The hoop force of the pinned-pinned arch with different temperature rises.

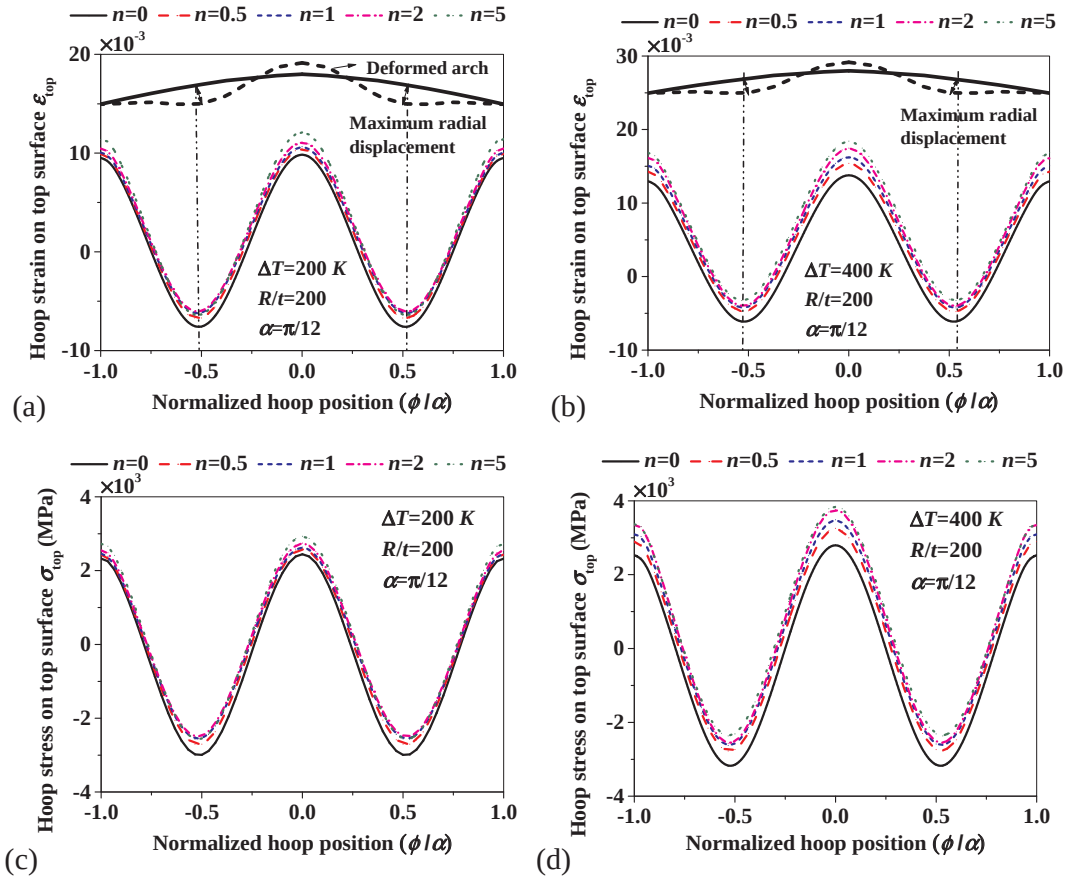

Fig. 21. The distribution of strain and stress at the top surface of the clamped-clamped arch.

Nevertheless, the volume fraction exponent, as well as the temperature rise, show small effects on the crown compressive stress and strain. In the middle surface, it is found the hoop strain is positive whereas the stress is negative and compressive as shown in Fig. 23. This is induced by the nature of thermal stresses. It should be noted that the case of $n = 0$ shows different strain and stress distributions from other cases because the material property of $n = 0$ is uniform in the cross-section. However, for other cases ($n = 0.5, 1, 2, 5$), additional hoop stress and strain are generated due to the non-symmetrical distribution of the material properties with respect to the middle surface of the FGM arches.

Figs. 24–26 depict the distribution of the hoop strain and stress at the top, bottom and middle surfaces of the pinned-pinned arch. Like the clamped-clamped cases, the maximum tensile strain and stress occur at the crown whereas the maximum compressive strain and stress occur at the maximum radial displacement position of the top surface in Fig. 24. On the contrary, the maximum compressive strain and stress occur at the crown whereas the maximum tensile strain and stress occur at the maximum radial displacement position of the bottom surface in Fig. 25. At the middle surface, all hoop strains are positive and change slightly through the arch span as shown in Fig. 26. The hoop stresses are compressive, which is similar to the clamped-clamped arches.

Figs. 27 and 28 illustrate the distribution of hoop strain and stress in the thickness direction of the mid-span ($\phi/\alpha = 0$). All strain and stress correspond to the critical buckling level. It is seen that the hoop strain is distributed linearly in the thickness direction for both clamped-clamped

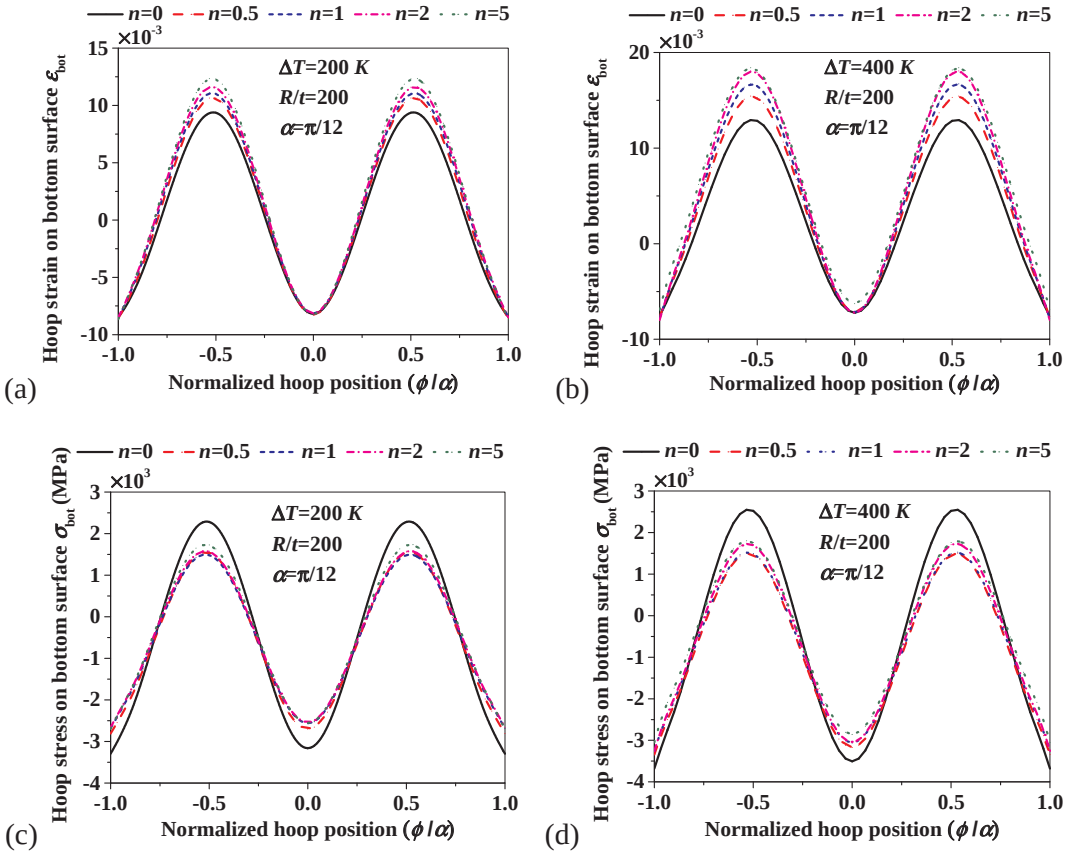

Fig. 22. The distribution of strain and stress at the bottom surface of the clamped-clamped arch.

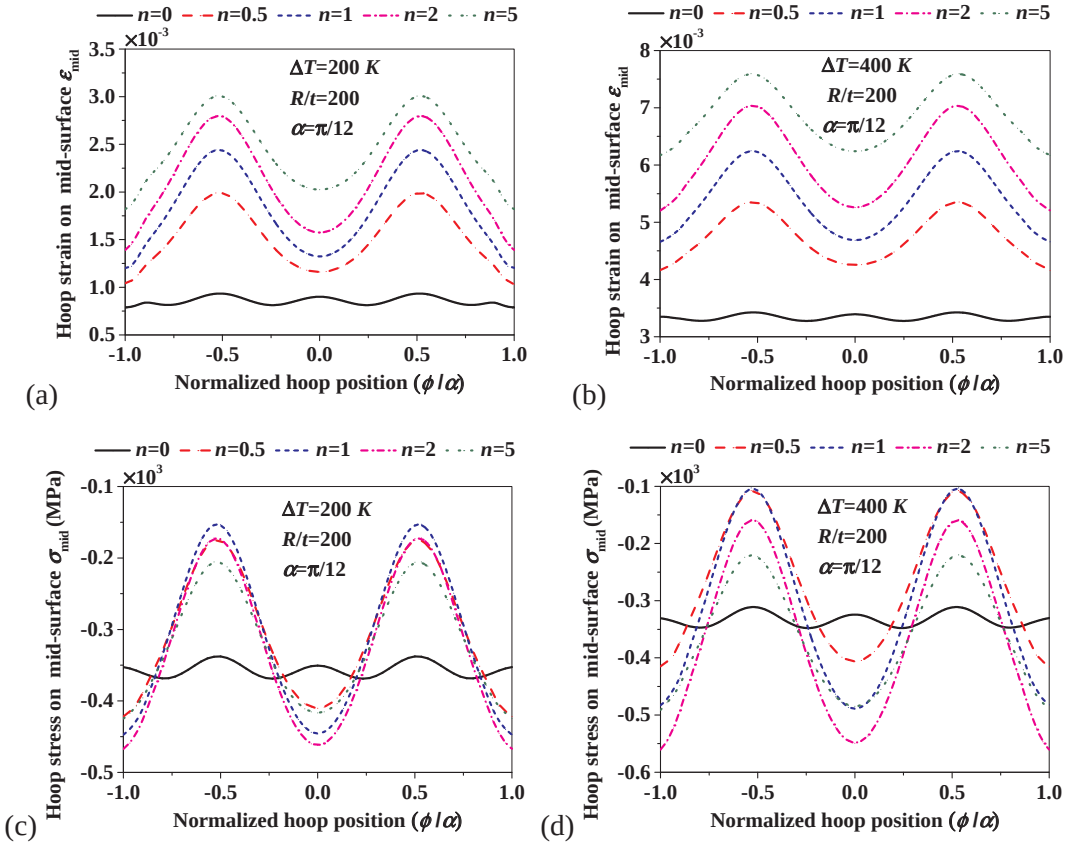

Fig. 23. The distribution of strain and stress at the middle surface of the clamped-clamped arch.

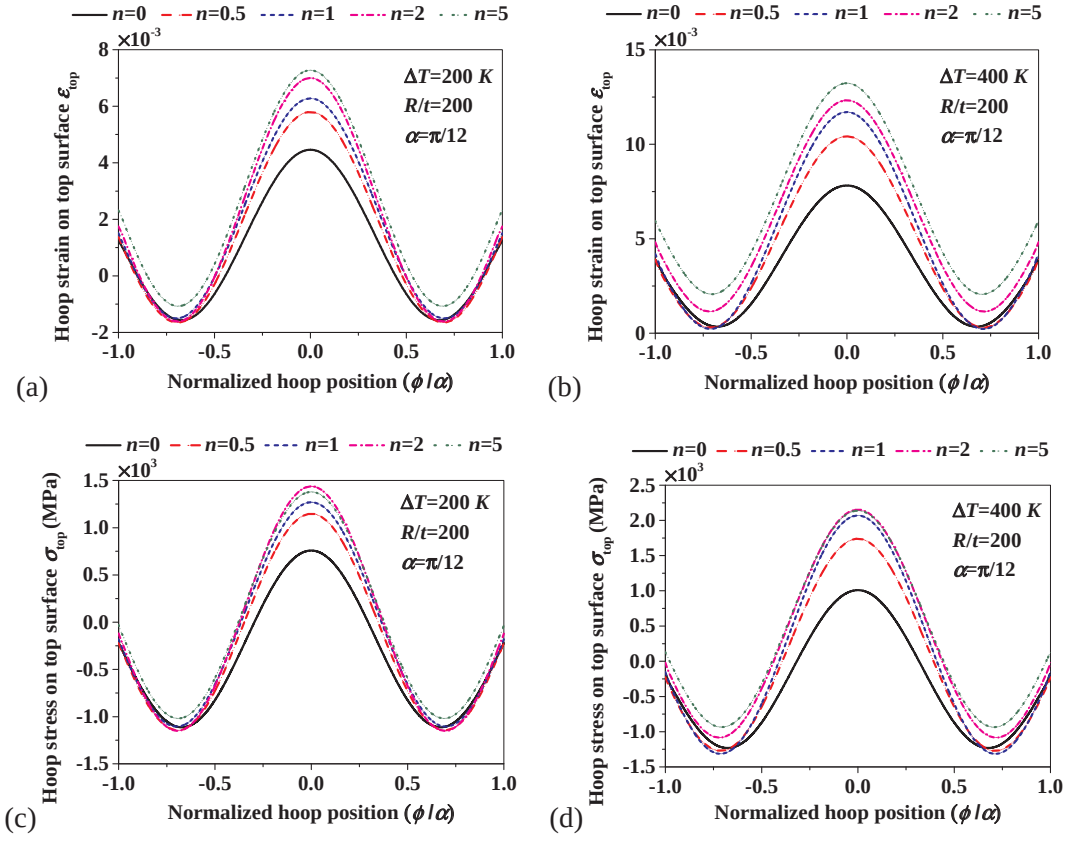

Fig. 24. The distribution of strain and stress at the top surface of the pinned-pinned arch.

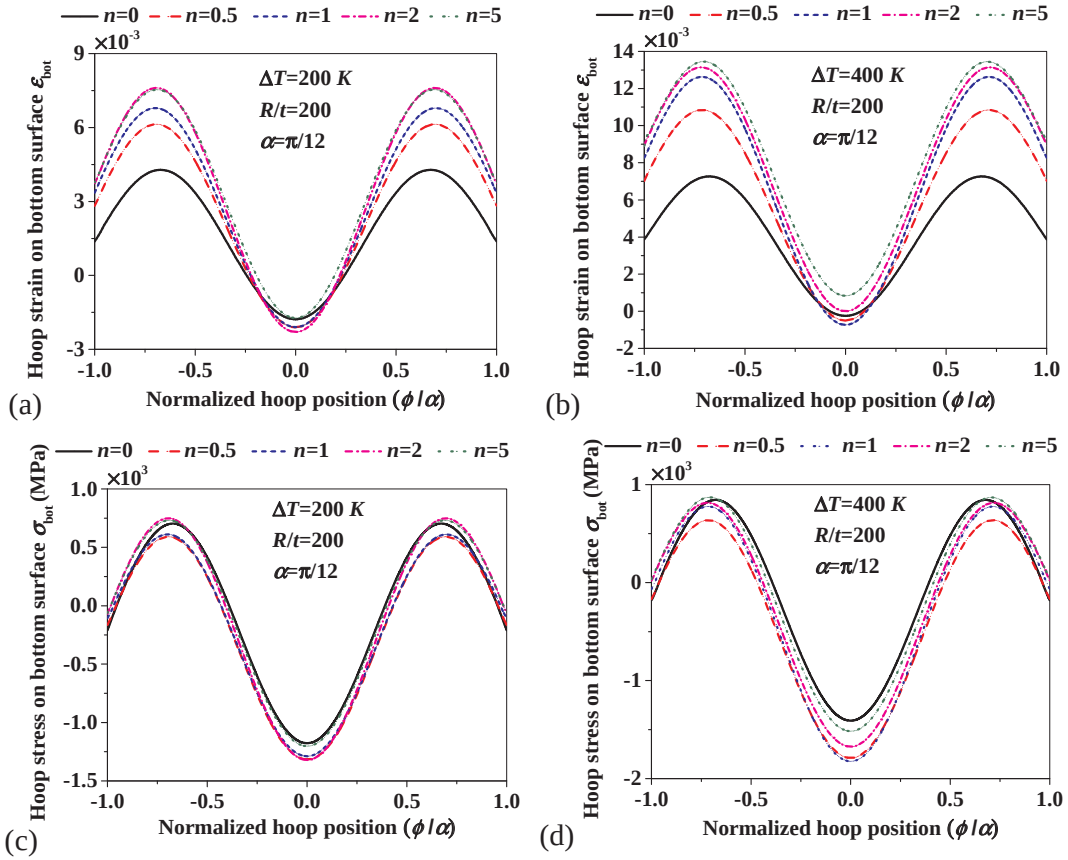

Fig. 25. The distribution of strain and stress at the bottom surface of the pinned-pinned arch.

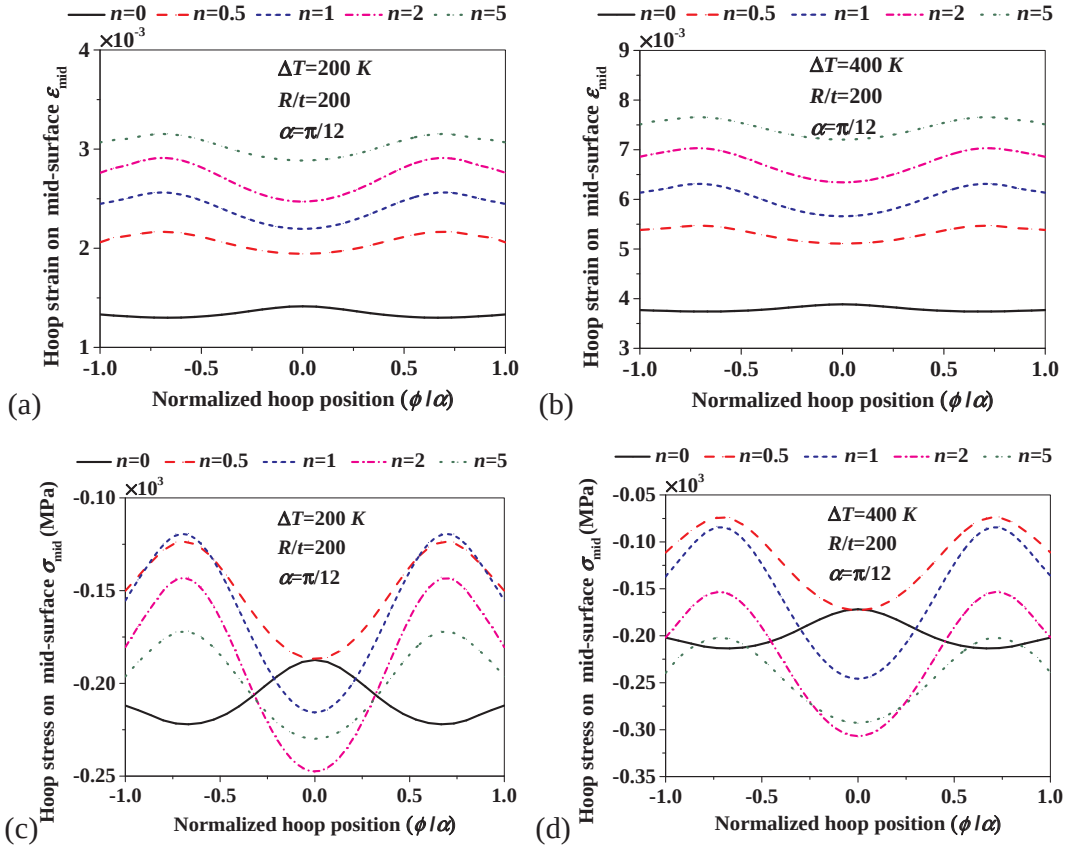

Fig. 26. The distribution of strain and stress at the middle surface of the pinned-pinned arch.

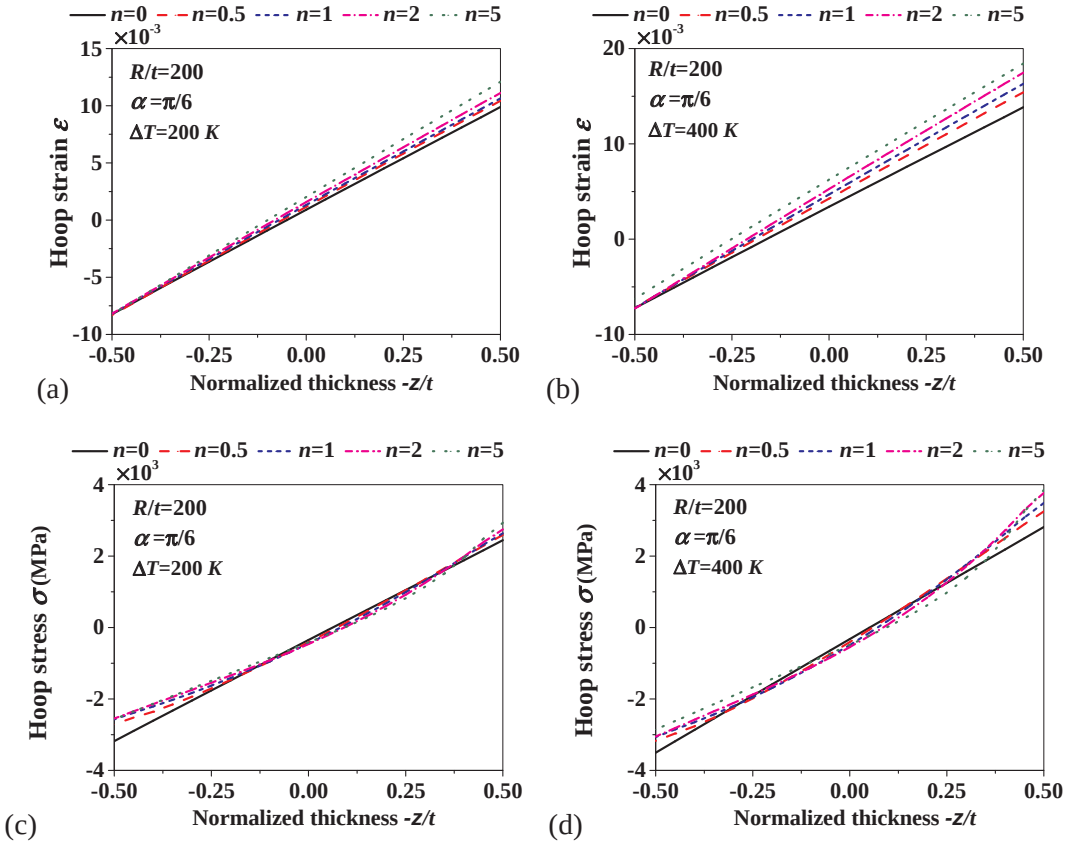

Fig. 27. Distribution of mid-span strain and stress in the thickness direction for the clamped-clamped arch.

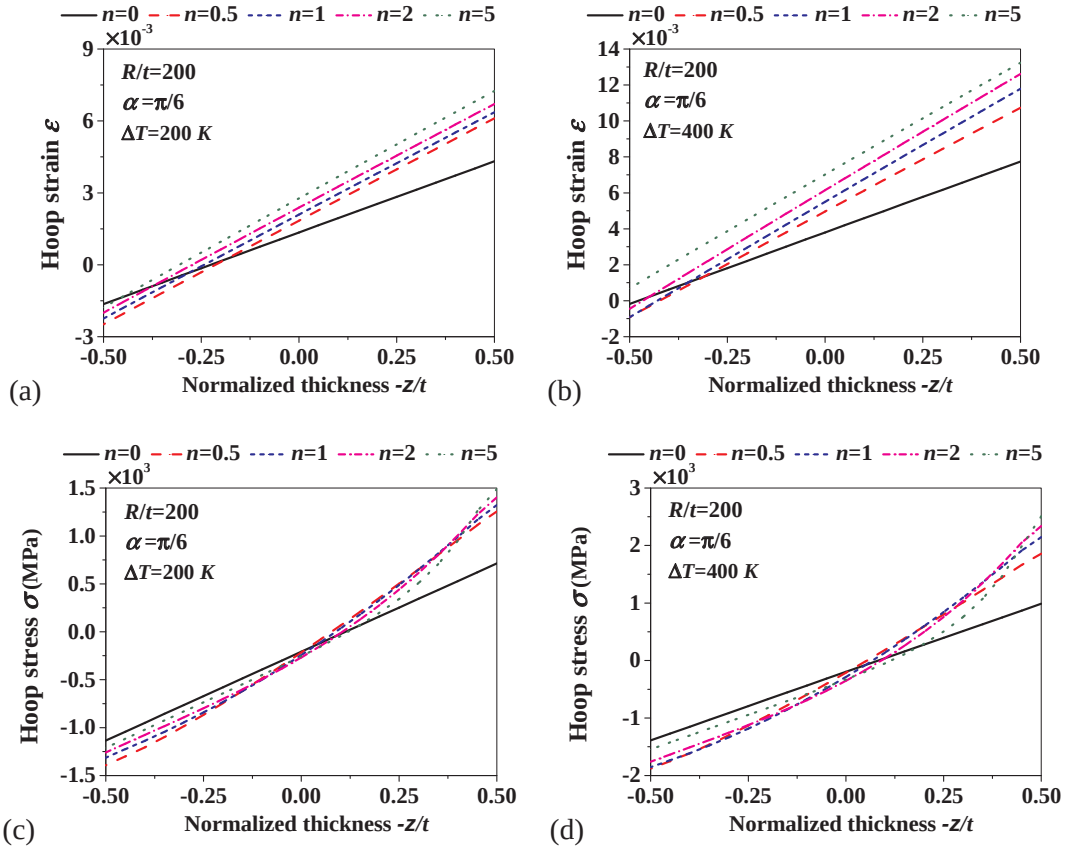

Fig. 28. Distribution of mid-span strain and stress in the thickness direction for the pinned-pinned arch.

and pinned-pinned arches, respectively. Generally, the higher the temperature, the higher the hoop strain and stress. Similarly, the higher the volume fraction exponent, the higher the hoop strain except for the vicinity of the bottom surface. However, the stress is distributed non-linearly due to the non-symmetrical dispersion of Young's modulus in the thickness direction ($n > 0$). For a homogeneous arch ($n = 0$), the stress is linear in the thickness direction.

5. Conclusions

The stability mechanism of the FGM arch is evaluated when it is subjected to external pressure and thermal loading. Based on the present analytical and numerical investigation, several main conclusions are emphasized:

(1) The derived analytical buckling pressure is verified successfully by the numerical results for both clamped-clamped and pinned-pinned arches, respectively. For a homogenous arch ($n = 0$), the present analytical and numerical results are consistent with available other closed-form expressions.
(2) The strain and stress of the FGM arch ($n > 0$) are distributed differently from the homogeneous arch due to the non-symmetrical distribution of the material properties in the cross-section.
(3) The temperature rise generates a thermal radially-outward displacement and a reduction on Young's modulus, which are positive and negative to the critical buckling pressure of the FGM arch, respectively.
(4) The layer number $N = 20$ in the thickness direction is accurate enough to converge the buckling pressure. Therefore, $N = 20$ is recommended to industrial manufacturing of the thin-walled FGM structures.

The present investigation is mainly concerned with the elastic buckling of the FGM arch. Further experimental verification is necessary before it is applied to engineering applications. In addition, the inelastic material properties are ignored in the present model. However, they may exist in practical systems and have significant effects on the buckling pressure.

Acknowledgements

The authors would like to thank the financial support from the Department of Civil, Construction and Environmental Engineering of Iowa State University.

Declaration of Competing Interest

The authors declare the present investigation has no conflict of interests with any other works or studies.

References

[1] Bradford MA. In-plane nonlinear behaviour of circular pin-ended arches with elastic restraints under thermal loading. Int J Struct Stab Dy 2006;6(2):163–77.
[2] Bradford MA. Long-span shallow steel arches subjected to fire loading. Adv Struct Eng 2010;13(3):501–11.
[3] Heidarpour A, Abdullah AA, Bradford MA. Non-linear thermoelastic analysis of steel arch members subjected to fire. Fire Safety J 2010;45:183–92.
[4] Han Y, Sun B, Ju Z, Wang Y. Critical load analysis of double-hinged circular steel arch in-plane under high temperature of the fire. Adv Mater Res 2011;243–249:3–6.
[5] Rastgo A, Shafie H, Allahverdizadeh A. Instability of curved beams made of functionally graded material. Int J Mech Mater Des 2005;2:117–28.
[6] Cai J, Xu Y, Feng J, Zhang J. Effects of temperature rises on the in-plane stability of steel arch bridges. J Bridge Eng 2012;17(2):232–40.
[7] Bouras Y, Vrcelj Z. Non-linear in-plane buckling of shallow concrete arches subjected to combined mechanical and thermal loading. Eng Struct 2017;152:413–23.
[8] Yan ST, Shen X, Chen Z, Jin Z. On buckling of non-uniform shallow arch under a central concentrated load. Int J Mech Sci 2017;133:330–43.

[9] Schreyer HL, Masur EF. Buckling of shallow arches. J Eng Mech Div 1966;92(EM4):1–19.
[10] Schmidt R, DaDeppo DA. Buckling of clamped circular arches subjected to a point load. J Appl Math Phys (ZAMP) 1972;23:146–8.
[11] Li Z, Zheng J, Sun Q, He H. Nonlinear structural stability performance of pressurized thin-walled FGM arches under temperature variation field. Int J Non-linear Mech 2019;113:86–102.
[12] Li Z, Tang F, Chen Y, Zheng J. Material distribution optimization of functionally graded arch subjected to external pressure under temperature rise field. Thin-walled Struct 2019;138:64–78.
[13] Garland JC, Tanner DB. Electron transport and optical properties of inhomogeneous media. New York: American Institute of Physics; 1978.
[14] Kocatürk T, Akbas SD. Post-buckling analysis of Timoshenko beams made of functionally graded material under thermal loading. Struct Eng Mech 2012;41(6):775–89.
[15] Asgari H, Bateni M, Kiani Y, Eslami MR. Non-linear thermo-elastic and buckling analysis of FGM shallow arches. Compos Struct 2014;109:75–85.
[16] Bateni M, Eslami MR. Non-linear in-plane stability analysis of FGM circular shallow arches under central concentrated force. Int J Non-linear Mech 2014;60:58–69.
[17] Swaminathan K, Naveenkumar DT, Zenkour AM, Carrera E. Stress, vibration and buckling analyses of FGM plates-A state-of-the-art review. Compos Struct 2015;120:10–31.
[18] Simsek M. Buckling of Timoshenko beams composed of two-dimensional functionally graded material (2D-FGM) having different boundary conditions. Compos Struct 2016;149:304–14.
[19] Moita JS, Araújo AL, Correia VF, Soares CMM, Herskovits J. Material distribution and sizing optimization of functionally graded plate-shell structures. Compos Part B 2018;142:263–72.
[20] Al-shujairi M, Mollamahmutoğlu C. Buckling and free vibration analysis of functionally graded sandwich microbeams resting on elastic foundation by using nonlocal strain gradient theory in conjunction with higher order shear theories under thermal effect. Compos Part B 2018;154:292–312.
[21] Xi S, Li SR. Nonlinear stability of clamped-clamped FGM arches subjected to mechanical and thermal loading. In: Yang W, Geni M, Wang TJ, Zhuang Z, editors. Advances in fracture and materials behaviour part 1-2. Proceedings of the seventh international conference on fracture and strength of solids (Urumqi, P.R. China, August 27-29, 2007). Stafa-Zurich, Switzerland: Trans Tech Publications Ltd.; 2008. p. 699–705.
[22] Pi YL, Bradford MA. Nonlinear in-plane elastic buckling of shallow circular arches under uniform radial and thermal loading. Int J Mech Sci 2010;52(1):75–88.
[23] Timoshenko SP, Gere JM. Theory of elastic stability. NewYork: McGraw-Hill; 1970.
[24] Wicks PJ. General equations for buckling of thin, shallow arches of any shape. J Eng Mech 1991;117(2):225–40.
[25] Bradford MA, Uy B, Pi YL. In-plane elastic stability of arches under a central concentrated load. J Eng Mech 2002;128(7):710–9.
[26] Li Z, Wang L, Guo Z, Shu H. Elastic buckling of cylindrical pipe linings with variable thickness encased in rigid host pipes. Thin-walled Struct 2012;51:10–9.
[27] Li Z, Zheng J, Wang R. Effects of grouting voids on the elastic buckling of confined pipe liners subjected to uniform pressure. Thin-walled Struct 2019;137:502–14.
[28] Li Z, Tang F, Chen Y, Tang Y, Chen G. Elastic and inelastic buckling of thin-walled steel liners encased in circular host pipes under external pressure and thermal effects. Thin-walled Struct 2019;137:213–23.
[29] Boot JC. Elastic buckling of cylindrical pipe linings with small imperfections subjected to external pressure. Trenchless Technol Res 1998;12(1–2):3–15.
[30] Wang JH, Koizumi A, Yuan DJ. Theoretical and numerical analyses of hydrostatic buckling of a noncircular composite liner with arched invert. Thin-walled Struct 2016;102:148–57.
[31] Boot JC, Naqvi MM, Gumbel JE. A new method for the structural design of flexible liners for gravity pipes of egg-shaped cross section: Theoretical considerations and formulation of the problem. Thin-walled Struct 2014;85:411–8.
[32] Praveen GN, Reddy JN. Nonlinear transient thermoelastic analysis of functionally graded ceramic-metal plates. Int J Solids Struct 1998;35(33):4457–76.
[33] Li Z, Tang Y, Tang F, Chen Y, Chen G. Elastic buckling of thin-walled polyhedral pipe liners encased in a circular pipe under uniform external pressure. Thin-walled Struct 2018;123:214–21.
[34] Allen HG, Bulson PS. Background to buckling. London: McGraw-Hill; 1980.
[35] ABAQUS, User's Manual: Version 6.12, Simulia, United States; 2013.
[36] Kiani Y, Eslami MR. Thermomechanical buckling of temperature-dependent FGM beams. Lat Am J Solids Struct 2013;10(2):223–46.
[37] Li Z, Zheng J, Chen Y. Nonlinear buckling of thin-walled FGM arch encased in a rigid confinement subjected to external pressure. Eng Struct 2019;186:86–95.
[38] Li Z, Wang R, Chen Y. Theoretical and numerical analysis of the structural stability of the pipe-grout-liner system with a crown void subjected to external pressure. Compos Part B 2019;173. 106944.
[39] Li Z, Zheng J, Meng L, Zou X, Hu X. Nonlinear stability analysis of thin-walled steel pipe confined in soft bilayer medium. Eng Struct 2019;196. 109318.
[40] Li Z, Tang F, Chen Y. Stability of the pipe-liner system with a grouting void surrounded by the saturated soil. Eng Struct 2019;196. 109284.
[41] Pi YL, Bradford MA, Guo YL. Revisiting nonlinear in-plane elastic buckling and post-buckling analysis of shallow circular arches under a central concentrated load. J Eng Mech 2016;142(8):04016046.